

**SEISMIC FAULTS DETECTION USING SALIENCY
MAPS**

BY

ABDULMAJID LAWAL

A Thesis Presented to the
DEANSHIP OF GRADUATE STUDIES

KING FAHD UNIVERSITY OF PETROLEUM & MINERALS

DHAHRAN, SAUDI ARABIA

In Partial Fulfillment of the
Requirements for the Degree of

MASTER OF SCIENCE

In

ELECTRICAL ENGINEERING

MAY-2016

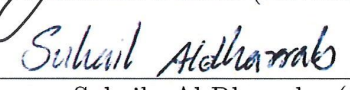
KING FAHD UNIVERSITY OF PETROLEUM & MINERALS
DHAHRAN 31261, SAUDI ARABIA

DEANSHIP OF GRADUATE STUDIES


This thesis, written by **ABDULMAJID LAWAL** under the direction of his thesis adviser and approved by his thesis committee, has been presented to and accepted by the Dean of Graduate Studies, in partial fulfillment of the requirements for the degree of **MASTER OF SCIENCE IN ELECTRICAL ENGINEERING**.

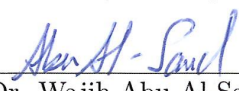
Thesis Committee


Dr. Mohamed Deriche (Adviser)

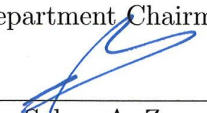

Dr. Suhail Al-Dharrab (Co-adviser)


Dr. Mohamed Mohandes (Member)


Dr. Ali Muqaibel (Member)


Dr. Wajih Abu-Al-Saud (Member)


Dr. Ali Al-Shaikhi
Department Chairman


Dr. Salam A. Zummo
Dean of Graduate Studies

2/6/16
Date



©Abdulmajid Lawal
2016

*I dedicate this thesis to Allah (S.W.A) for keeping me alive and
guiding me to the straight path.*

ACKNOWLEDGMENTS

All thanks and praises be to Allah (SWT), and may peace and blessings be upon the prophet Muhammad (PBUH), his family, his companions and his followers.

I want to use this great opportunity to express my sincere gratitude to my advisor Dr. Mohamed Deriche and my co-advisor Dr. Suhail Al-Dharrab for their unrelenting and unwavering support and guidance from the beginning to the end of my Masters thesis. For their understanding, continual encouragement, motivation, new ideas, and intellectual support.

I also like to express deep appreciation to my parents and family members, for their prayers, love, support, compassion, advice, and encouragement that served as a constant source of motivation without which this work would not have been possible.

To my friends for providing the work distraction necessary to bring balance and richness to my masters program experience.

To my committee members, Dr. Mohamed Mohandes, Dr. Ali Muqaibel, Dr. Wajih Abu-al-Saud for providing fruitful suggestions at the very beginning that helped in the focus of the thesis work.

Finally, I wish to acknowledge King Fahd University of Petroleum and Minerals (KFUPM) for given me the opportunity to study and providing the neces-

sary working environment that facilitated my studies. I also thank my employers Bayero University Kano, Nigeria (BUK) for allowing me to further my studies.

TABLE OF CONTENTS

ACKNOWLEDGEMENT	iii
LIST OF TABLES	viii
LIST OF FIGURES	ix
ABSTRACT (ENGLISH)	xiii
ABSTRACT (ARABIC)	xv
CHAPTER 1 INTRODUCTION	1
1.1 Background	2
1.2 2D /3D Seismic Data	4
1.3 Seismic Imaging	6
1.4 Seismic Faults	8
1.5 Seismic Data Interpretation	9
1.6 Experimental Data	10
1.7 Thesis Motivations and Objectives	11
1.8 Thesis Contributions	12
1.9 Thesis Outline	12
CHAPTER 2 LITERATURE REVIEW	13
2.1 Fault Detection in 2D and 3D Data set	14
2.1.1 Fault Detection Based on The Hough Transform	15

2.1.2	Fault Detection Based on Ant Colony Optimization Algorithms	19
2.1.3	Fault Detection Based on Directional Filters	21
2.1.4	Fault Detection Based on Active Contour	22
2.1.5	Fault Detection Based on Skelotonization	23
2.1.6	Other Methods for Fault Detection	24
2.2	Visual Saliency Models	26
2.3	Saliency Estimation	29
2.3.1	Biological Models	30
2.3.2	Purely Computational Models	31
2.3.3	Hybrid Models	33
CHAPTER 3 SEISMIC ATTRIBUTES		34
3.1	Coherence Attribute	36
3.1.1	Semblance-based Coherence	37
3.1.2	Variance-based Coherence	39
3.1.3	Eigenstructure-based Coherence	41
3.2	Curvature Attributes	42
3.3	Curvature in 2D Cross-Sections	43
3.3.1	Most Positive and Most Negative Curvature	44
3.4	Dip Attribute	46
3.4.1	Weighted Dip	49
3.5	Gradient Attribute	50
3.6	Other Fault Enhancing Attributes	51
CHAPTER 4 A SALIENCY-BASED MODEL FOR FAULT DETECTION		53
4.1	Proposed Fault Detection Model	54
4.2	Covariance Matrix for The Meta Feature	55
4.3	Feature Integration using Region Covariance	56
4.4	Region Covariance	56

4.5	Local Saliency Estimation	58
4.6	The Saliency Model	59
4.7	Implementation details	61
4.8	Conclusion	72
CHAPTER 5 DELINEATING FAULT LINES		74
5.1	Fault Enhancement	74
5.2	Global Thresholding	76
5.3	Numerical Optimization	80
5.4	Labeling Faults	83
5.5	Similarity Index Measurement	85
CHAPTER 6 CONCLUSION AND FUTURE WORK		91
6.1	Conclusion	91
6.2	Future work	92
REFERENCES		93
VITAE		104

LIST OF TABLES

4.1	Table of Parameters	62
-----	-------------------------------	----

LIST OF FIGURES

1.1	Seismic acquisition using a vibrator truck, geophones and recording truck [5].	3
1.2	A 2D seismic section with faults [5].	5
1.3	A 3D seismic section with faults [5].	6
1.4	A 3D seismic data with Inline, Crossline, and Depth directions [7].	7
1.5	Different types of faults [1].	9
2.1	The image space and the parametric space [1].	16
2.2	(a) The infinite lines produced by the method used in [9], (b) The background noise produced by method in [9].	17
2.3	(a) Bottom up saliency scenario (b) Top down saliency scenario . .	27
2.4	(a) A bicycle as the prominent object (b) Saliency map highlighting the bicycle.	28
3.1	(a) Inline 257 (b) Inline 272 and (c) Inline 249 from the F3 dataset.	36
3.2	The semblance based coherence of (a) inline 256 (b) inline 272 (c) inline 249.	39
3.3	The variance based coherence of (a) inline 256 (b) inline 272 (c) inline 249.	40
3.4	The eigenstructure based coherence of (a) inline 256 (b) inline 272 (c) inline 249.	42
3.5	2D illustration of curvature at different point in a surface.	43
3.6	The most positive curvature attribute of (a) inline 256 (b) inline 272 (c) inline 249.	45

3.7	The most negative curvature of (a) inline 256 (b) inline 272 (c) inline 249.	46
3.8	The dip of (a) inline 256 (b) inline 272 (c) inline 249.	49
3.9	The weighted dip of (a) inline 256 (b) inline 272 (c) inline 249. . .	50
3.10	The gradient of (a) inline 256 (b) inline 272 (c) inline 249.	51
4.1	Block diagram of the proposed workflow.	54
4.2	A synthetic image illustrating the non overlapping block decomposition.	59
4.3	Seismic section, inline 256.	62
4.4	The saliency map of the attributes of inline 256 (a) Coherence (b) Curvature (c) Dip (d) Gradient.	63
4.5	Seismic section, inline 256.	63
4.6	The saliency map of the attributes of inline 272 (a) Coherence (b) Curvature (c) Dip (d) Gradient.	64
4.7	Combined saliency map of inline 256.	65
4.8	Combined saliency map of inline 272.	65
4.9	(a) inline 256 (b) overlaid saliency map.	66
4.10	(a) inline 272 (b) overlaid saliency map.	67
4.11	Seismic section, inline 249.	67
4.12	Saliency map of the attributes for inline 249 (a) Coherence (b) Curvature (c) Dip (d) Gradient.	68
4.13	Combined saliency map for inline 249.	68
4.14	(a) Inline 249 (b) overlaid saliency map.	69
4.15	(a) inline 258 (b) overlaid saliency map.	69
4.16	(a) inline 260 (b) overlaid saliency map.	70
4.17	(a) inline 262 (b) overlaid saliency map.	70
4.18	(a) inline 264 (b) overlaid saliency map.	70
4.19	(a) inline 266 (b) overlaid saliency map.	71
4.20	(a) inline 268 (b) overlaid saliency map.	71

4.21	(a) inline 270 (b) overlaid saliency map.	71
4.22	(a) inline 280 (b) overlaid saliency map.	72
4.23	(a) inline 290 (b) overlaid saliency map.	72
5.1	Variance-based coherence of (a) inline 256 (b) inline 272.	75
5.2	Most-negative curvature of (a) inline 256 (b) inline 272.	76
5.3	Binary image for inline 256 after (a) thresholding $c_v(x, y)$ (b) false feature removal.	77
5.4	Binary image for inline 272 after (a) thresholding $c_v(x, y)$ (b) false feature removal.	78
5.5	Connected points after false feature removal for (a) inline 256 (b) inline 272.	80
5.6	Optimization using variance-based coherence for (a) inline 256 (b) inline 272.	82
5.7	Optimization using curvature for (a) inline 256 (b) inline 272. . .	83
5.8	Optimization using both variance-based coherence and curvature attributes for (a) inline 256 (b) inline 272.	83
5.9	Labeled faults for (a) inline 256 (b) inline 272.	84
5.10	Proposed labeled faults (green) compared with ground truth (red) for (a) inline 256 (b) inline 272.	84
5.11	The labelled faults of inline 249 with multiple fault.	85
5.12	SalSIM indices of the proposed method (green) with the Hough transform based method in [1] (red).	86
5.13	(a) inline 258 (b) Proposed labelled faults (green) compared with ground truth (red) for inline 258	87
5.14	(a) inline 260 (b) Proposed labelled faults (green) compared with ground truth (red) for inline 260	87
5.15	(a) inline 262 (b) Proposed labelled faults (green) compared with ground truth (red) for inline 262	88

5.16	(a) inline 264 (b) Proposed labelled faults (green) compared with ground truth (red) for inline 264	88
5.17	(a) inline 266 (b) Proposed labelled faults (green) compared with ground truth (red) for inline 266	89
5.18	(a) inline 268 (b) Proposed labelled faults (green) compared with ground truth (red) for inline 268	89
5.19	(a) inline 274 (b) Proposed labelled faults (green) compared with ground truth (red) for inline 274	90

THESIS ABSTRACT

NAME: Abdulmajid Lawal
TITLE OF STUDY: Seismic Faults Detection Using Saliency Maps
MAJOR FIELD: Electrical Engineering
DATE OF DEGREE: May, 2016

Seismic data acquisition is usually associated with large amounts of data collected from surveys. Due to the high demand of oil, seismic surveys are conducted in onshore, offshore and even previously exploited regions in order to look for additional reservoirs. Seismic data set can easily add up to hundreds of gigabytes in size which is forcing the oil industry to find an alternative option to traditional manual interpretation. Interpretation is associated with the efficient extraction of seismic features such as salt dome and faults that have the potential of indicating the presence of hydrocarbon. Here, we propose a novel saliency-based approach using different seismic attributes such as coherence, gradient, curvature and dips in parallel. Each attribute is calculated independently from the original seismic section. The saliency map which highlights the fault region is computed for all the aforementioned attributes using a covariance matrix, the saliency maps are

later combined linearly to form a consolidated saliency map that highlights the fault region. The covariance matrix is used to characterize the seismic patches and captures local structures. By thresholding the variance maps and optimizing the binary points for curve fitting, the fault location is labelled. The proposed approach performs well as the labelled fault is very close to the ground truth and the SalSIM index (a frechet distance based algorithm that measures the distance between ground truth and labelled fault) was close to unity.

CHAPTER 1

INTRODUCTION

A fault is a common geological structure formed by a displacement between neighbouring tectonic plates. Under normal conditions, the porous reservoir rocks are sealed by faults and lead to the formation of petroleum reservoirs. Typically, seismic data sets contain significant amount of faults at different scales. One of the critical keys to understand and properly analyze geological data is the knowledge of the particular locations of faults in the subsurface. The fact that faults act as a seal to the movement of crude oil is of major economic significance.

Therefore, accuracy in locating faults is essential in order to maximize the efficiency of oil production by planning drilling sites effectively [2]. Although, significant progress has been made in the development of automatic fault tracking algorithms, current techniques depend mainly on manual procedures which involve slice by slice handpicking of discontinuities over a seismic image, one fault at a time. This task is time consuming even for well-trained interpreters who have to interpret hundreds of seismic surveys. Hence, there is an obvious needs to

put extensive research efforts in developing automatic or semi automatic fault detection techniques. This problem however, is practically difficult due to imaging artefacts, noise and a significant number of faults interacting together at different spatial scales [3].

In this work, we propose a new bottom-up approach that highlights the fault regions using the concept of saliency map based on different seismic attributes. The saliency maps are then used to focus on fault regions and eliminate the unimportant parts of the image. By applying an adaptive thresholding to the resulting variance-based saliency map, we precisely locate the faults. Furthermore, we used the variance-based coherence and curvature attributes to further optimize and label the fault points in the seismic section. We show that the proposed approach detects faults accurately at a reduced computational cost compared to existing techniques.

1.1 Background

Among the different techniques used for the analysis of geophysical surveys, seismic reflection is one of the most popular and widely used techniques in geophysics. Several geological details can be revealed by processing seismic reflection data on scales from a few meters of the earth crust to its inner core [4]. A geologist with a good understanding of how reflections are used and seismic sections are created, can perform interpretation manually. There are many applications in which the analysis of seismic data is performed these include earth core structure de-

termination, exploration of petroleum monitoring of earth quakes, etc. Seismic signals are generated by a source (transmitter), such as an explosion, vibroseis (vibrating truck that generates sound energy), which then propagates through earth layers. Some of these generated signals are refracted, reflected, and lost due to attenuation.

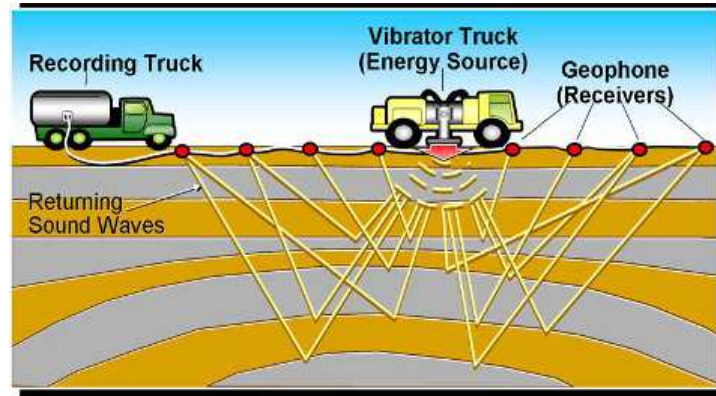


Figure 1.1: Seismic acquisition using a vibrator truck, geophones and recording truck [5].

The reflected signal is recorded by a set of receivers at the surface. Figure 1.1 shows a typical example of seismic acquisition, the vibrator truck generates sound waves that penetrate through the subsurface, along the line the waves get reflected and refracted, a series of geophone receivers are used to record the reflections, refractions, and diffractions of the returning waves and a recording truck records the travel times between the source and the receiver. Overall, seismic survey analysis is the task of collecting data using receiver arrays, transmitting data over a narrow band channel, and storing the data for processing, and finally, data interpretation; the data can be 2D or 3D depending upon the number of

sources and arrangements of the receivers (geophones) used during acquisition. The main focus is seismic interpretation is the extraction of subsurface geological information from seismic data such as faults, stratigraphic features, salt dome, fractures etc.

1.2 2D /3D Seismic Data

The subsurface geology can be viewed or imaged through seismic reflection by inducing acoustic wave from the surface of the earth and listening for the echoes. To record a 2D seismic data set, the receivers (geophones) are arranged in a straight line across the surface of the earth. An explosive device or vibroseis (vibrating truck) is used to generate acoustic energy. The generated energy travels through the subsurface as a spherical wave front. Since the rock layers beneath the earth surface are not perfectly elastic, some energy is reflected back while the remaining energy is transmitted to the next rock layer. The reflected signal at the surface is detected by the receivers and recorded by recording devices, Figure 1.2 shows a 2D seismic section with a fault indicated in circle.

In 3D seismic acquisition, more than one source is usually employed to generate the acoustic energy and the receivers are arranged in a square form across the earth surface. A group of shots is recorded sequentially between two receiver lines and centred with the patch (area of the receivers), Figure 1.3 an example of a 3D seismic volume.

It is worthy of note that before obtaining the final seismic images, a series

of processing steps are performed on the acquired data. These steps include filtering, deconvolution, velocity analysis, normal move-out correction, stacking and migration. The main aim of these processing steps is to reduce the noise level, improve temporal resolution, correct lateral variation in the velocity, improve thickness of weathering layer, and enhance spatial resolution [1]. In this work, our main focus is interpretation, we are mainly interested in the final image after the series of processes have been performed.

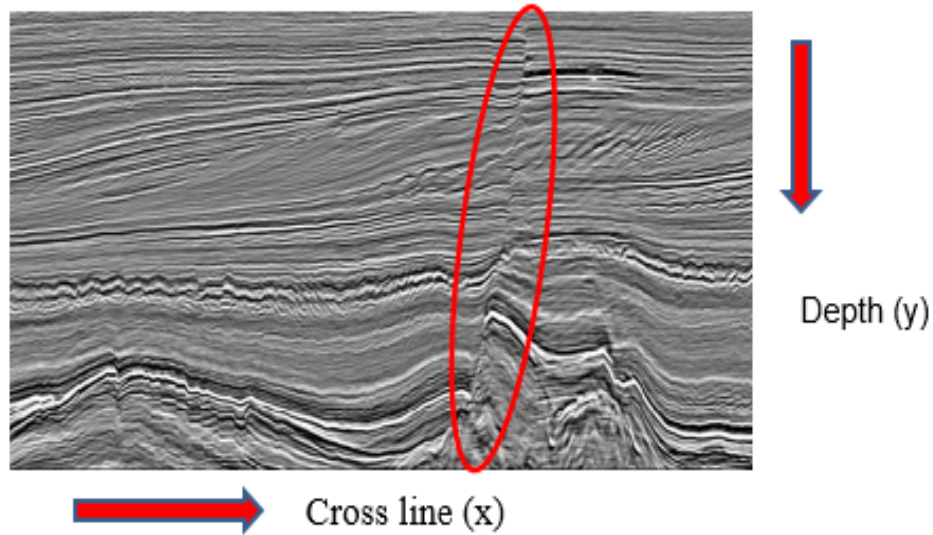


Figure 1.2: A 2D seismic section with faults [5].

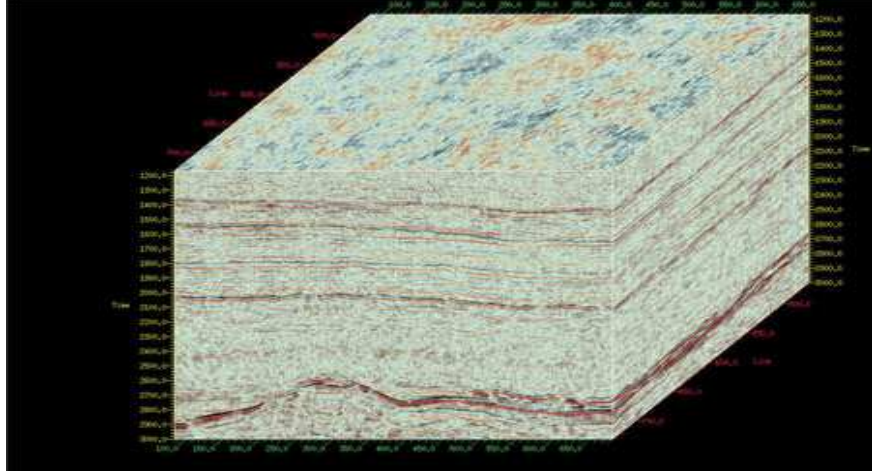


Figure 1.3: A 3D seismic section with faults [5].

1.3 Seismic Imaging

There are several ways for performing subsurface imaging. However, seismic imaging gives better details and therefore is very efficient in hydrocarbon exploration [5]. Seismic imaging is usually carried out at or near the surface of the earth in order to measure the elastic properties of the subsurface rocks as well as to detect the variations of such properties. The variations in seismic data are later employed to formulate a hypothesis about the underground rocks and fluids. Seismic imaging has the ability to capture the picture depth of up to 10 kilometers below the earth surface with spatially resolved features over tens of meters [5].

A conventional seismic data acquisition system is employed to generate images of the subsurface structure by recording the reflections of the wave from the rock layers. The amplitude and reflection times of the waves are recorded which are then used to formulate a hypothesis relating to depth and boundary properties

between rock layers. Seismic imaging gives useful information about hydrocarbon accumulation and helps in avoiding unnecessary drilling of exploratory wells. A typical 3D seismic data has several closely spaced seismic lines and provides a good measurement of subsurface reflectivity in the spatial space. Figure 1.4 shows the inline, crossline and time/depth direction of a 3D seismic data. The inline direction corresponds to the direction in which the data is acquired, the crossline direction corresponds to the direction orthogonal to the direction of acquisition and the time direction represents the depth of the subsurface structure. The time is measured in two-way travel time unit. The two-way travel time is the amount of time spent by the signal from the surface to the sublayer and back to the surface.

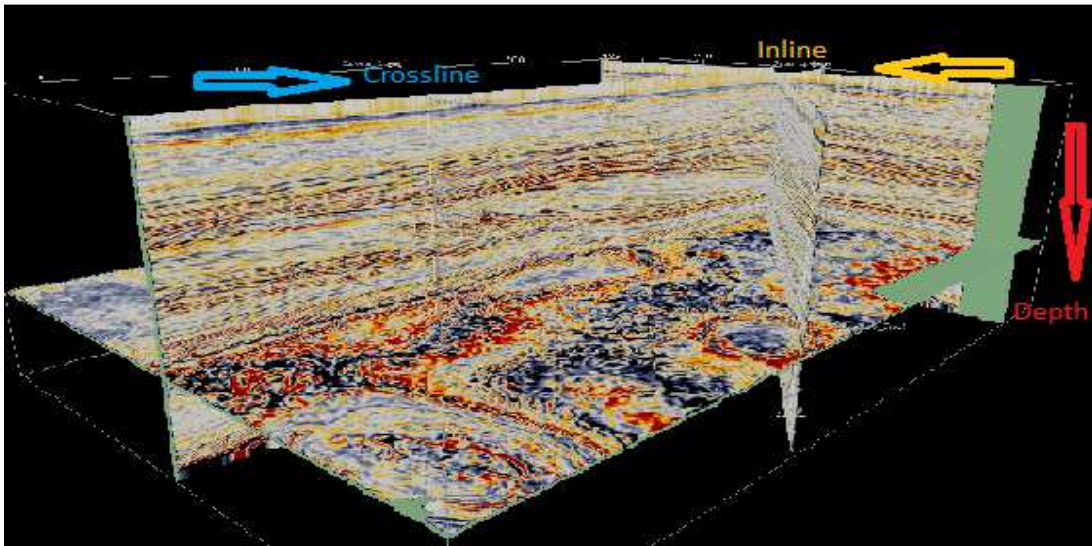


Figure 1.4: A 3D seismic data with Inline, Crossline, and Depth directions [7].

1.4 Seismic Faults

The concept of Fault is used to describe the movement of impermeable rocks opposite to the rocks with pore space formations which often contain oil and gas and creates traps. It is caused mainly by the shearing and offsetting of a strata. Both the tilt of the petroleum and the created fault, trap the oil and gas in the reservoir [6].

There are several types of faults, these include; normal, reverse, strike-slip, and thrust faults. As illustrated in Figure 1.5, a normal fault is a type of fault in which one side of the rock blocks drops down relative to the other side while reverse fault involve the push of one side of the rock blocks upward relative to the other side. In the case of strike slip fault, the rock blocks of each side slide along side-by-side. Finally, the thrust fault is formed when one side of the ground moves up and over adjacent ground. A number of studies have been conducted that formulate the relationship between rock displacement and fault geometry. A fault displacement is defined as an offset of points that were once continuous or adjacent. For a maximum displacement D and a fault length L , the relationship between them is given as $D \propto L^c$ for $1 \leq c \leq 2$.

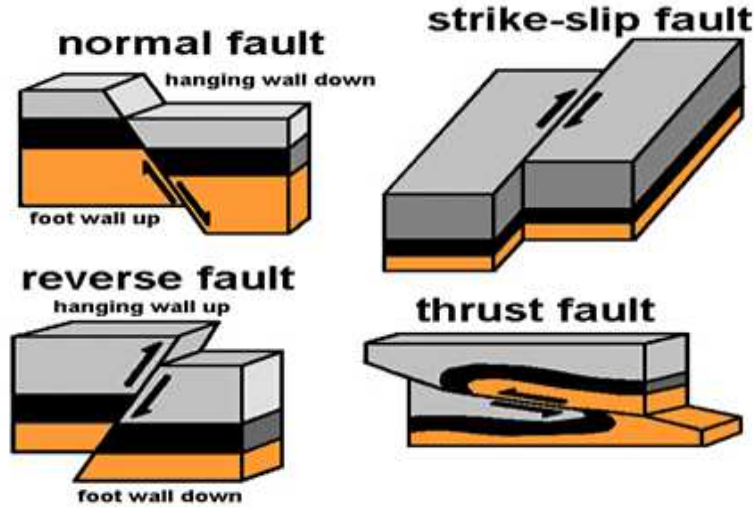


Figure 1.5: Different types of faults [1].

1.5 Seismic Data Interpretation

Seismic interpretation refers to the science of inferring the geology at some depth from the processed seismic record. The main aim of seismic interpretation is to detect certain features that trap hydrocarbon. While modern multichannel data has increased the quantity and quality of interpretable data, proper interpretation still requires that the interpreter draws upon his or her geological understanding to pick the most likely interpretation and decision from the multiple valid interpretations. The interpretation process can be sub-divided into three interrelated categories: structural, stratigraphic, and lithologic. The aim of seismic interpretation is to create structural maps of the subsurface from the observed three-dimensional configuration of arrival times. Seismic sequence stratigraphic interpretation relates the pattern of reflections observed to a model of cyclic episodes of deposition.

Lithology interpretation is aimed at determining changes in pore fluid, porosity, fracture intensity, lithology, and so on from seismic data. Direct hydrocarbon indicators (DHI, bright spots, or dim-outs) are commonly used as in this lithologic interpretation process. Seismic attributes are essential in this interpretation aspect as they can be used to enhance the discontinuity regions of seismic images [6]. Even though different approaches have been used in the field of interpretation, there is still a need to automate the process to save time and make it more accurate.

1.6 Experimental Data

3D seismic data can be analysed in three main directions which includes the inline, crossline and time (depth) directions. The inline is the direction of data acquisition, the cross line is the direction perpendicular to the inline, and the depth direction. In our experiments, we used the 3D seismic dataset obtained from the Netherlands offshore F3 block acquired in the North sea [7]. Our main focus is on the seismic volume which contains long and apparent faults that are located between inline range of 200 to 300, the crossline from 700 to 1200 and with a time range from 400 ms to 1100 ms. The data base is publicly available and has been extensively used in benchmarking different seismic interpretation applications and algorithms.

1.7 Thesis Motivations and Objectives

The major oil reservoirs are often associated with faults and the area covered by the survey increases over the years and hence data can get up to hundreds of gigabytes in size. The automation of faults detection and tracking enables the seismic interpreters to deal with larger amount of data effectively. This automatic analysis provides reliable measures, reduces bias and improves the speed and consistency of the workflow. Geophysics knowledge combined with both signal processing and image process techniques are seen as key to solve this problem. We aim to develop a new framework for detecting faults using a combination of attributes together with the concept of visual saliency so that the focus is only on areas interpreters looks for to make decisions on geological structures. The main aim of this work is to ease the work of an interpreter in locating faults in seismic data and to provide a more rapid convergence to the final interpretation result under practical scenarios. The main objectives of this thesis are as follows:

- To develop a fusion algorithm using different seismic attributes to enhance and detect fault regions in seismic data.
- To develop a saliency map based on seismic attributes that automatically stresses fault regions in seismic data.
- To automatically label fault regions in seismic data set using an optimization algorithm.

1.8 Thesis Contributions

- Development of an algorithm that automatically generates a saliency map for detecting faults using a combination of attributes.
- The development of an optimization technique that can be used to effectively track faults (one or more) in seismic datasets.
- Extensive experiments on real data that validate the proposed algorithms.

1.9 Thesis Outline

The thesis is organized around 6 chapters. Chapter 2 provides an overview of automatic fault detection in seismic data and discusses the concept of saliency and the various approaches used in modelling the human visual system. Chapter 3 explains the different types of seismic attributes able to enhance fault regions in seismic data. In Chapter 4, we provide our workflow in which the saliency of the different seismic attributes are computed to form a single saliency map which highlights the fault regions. Chapter 5 provides an effective way and computationally efficient algorithm that labels fault points using a thresholding and optimization techniques. Chapter 6 discusses our results and provide a final conclusion.

CHAPTER 2

LITERATURE REVIEW

Seismic faults are common geological structures formed by the transverse movement of rocks adjacent to each other disrupting the horizon continuity. Their detection is crucial in indicating possible petroleum reservoirs and facilitating bore-hole and well drillings. Seismic interpreters spend considerable efforts in locating faults after processing seismic data. Due to the massive nature of seismic data, adopting manual interpretation techniques is time consuming and expensive. Therefore, developing techniques that can identify faults automatically continues to be an active area of research. Many algorithms have been proposed in the literature for the detection of horizon discontinuities based on different seismic attributes, which can be further utilized to extract fault information.

In early studies most fault detection techniques are based on extracting edge information. Later, different image processing techniques have been introduced to tackle a number of interpretation problems indicating fault details. There are several algorithms that have been developed over the past few years that auto-

matically extract faults from seismic data including ant tracking algorithms [8, 9], machine learning [10], Hough transform [11, 12, 1, 13, 14], and directional filtering techniques [15], to mention a few. Generally, these techniques are applied to seismic sections after enhancing the discontinuity regions based on seismic attributes such as coherence[16, 17, 18], dips and azimuth[19, 20, 21], and curvature[22, 23]. A threshold is applied to convert the highlighted seismic section into an equivalent binary image, then an appropriate filter is applied before the final stage of labelling the fault lines/surfaces in 2D and 3D dataset, respectively.

First, we will discuss previous works on fault detection in 2D and 3D data sets using different image processing techniques. The second part discusses the concept of visual saliency and different saliency models that can be used to mimic the human visual system and can be applied in seismic data processing.

2.1 Fault Detection in 2D and 3D Data set

The main difference between 2D and 3D seismic data is the mode of acquisition and the resulting image produced. The 2D seismic acquisition is performed using one source with several receivers in straight lines resulting in so-called vertical seismic sections. On the other hand, 3D seismic acquisition is performed using a rectangular arrangements of receivers with more than one source resulting in a seismic volume. Different authors have attempted to develop algorithms that detect faults in 2D seismic data, some of these algorithms have been extended to 3D seismic sections. However, in some cases entirely new algorithms have been

developed for 3D seismic surveys. The most popular approaches are discussed below.

2.1.1 Fault Detection Based on The Hough Transform

One of the earliest works in detecting faults was based on the Hough transform. The Hough transform has been used in several image processing applications to extract features from digital images. It is capable of detecting specific shapes such as lines, ellipses or circles edge using a voting procedure [11]. It was introduced by Richard Duda and Peter Hart in 1972, and was first reportedly applied to detect fault in seismic sections by Albinhassan *et al.* [11]. In other to use the Hough transform, the coherence volume or other feature enhancing attributes are obtained first from the original seismic image, then a structural oriented filter is applied to filter out noise. Then, the binary data volume which is coded as 1 for the presence of fault and 0 for its absence is produced. During this stage, thresholding is used to filter out footprint noise. The Hough transform is then applied, where points in the image space are transformed into a curve in the parameter space and vice versa, the transform equation is given as :

$$x\cos(\theta) + y\sin(\theta) = r \quad (2.1)$$

where x and y are constants in the parameter space, and r and θ are constants in the image space. As shown in Figure 2.1, for any given point on the blue line r and θ are constants in the image space. For the curves in the parameter space x

and y are constants at any given point. Therefore, the intersection of curves in the parameter space corresponds to a line in the image space. Several authors have

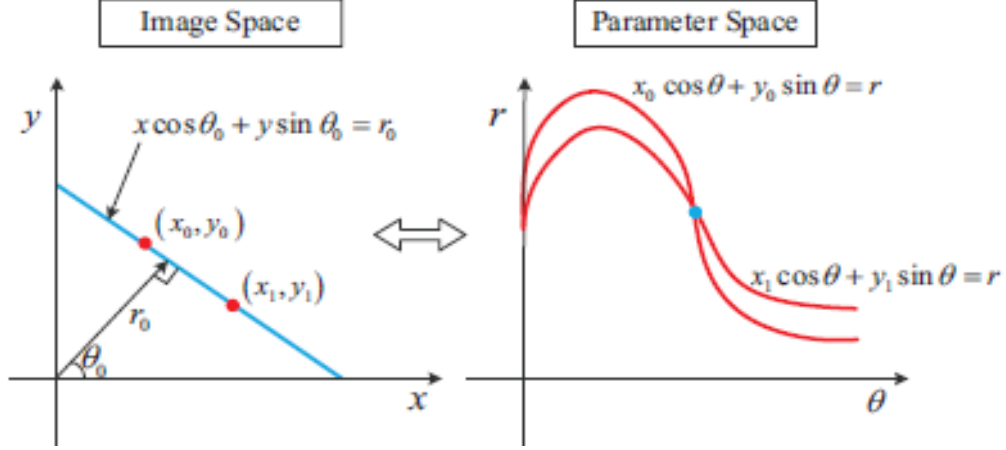


Figure 2.1: The image space and the parametric space [1].

used this method to detect fault lines in seismic sections. The Hough transform was implemented using a global and small running window. In the global method, the whole image was transformed into the polar space first, then, the new image was constructed while in the small running window method a certain window was used and the Hough transform was applied for each for the windows. Before the Hough transform a coherence cube [16] and curvature [22] of the seismic section are obtained respectively. In the experiment, the Hough transform was applied to the curvature enhanced seismic section using a small running window while it was applied to the coherence cube using a global window. Both methods perform well, the first method is sensitive to noise but the lines appear to be finite while the second type was robust against noise but the fault lines appear to be infinite.

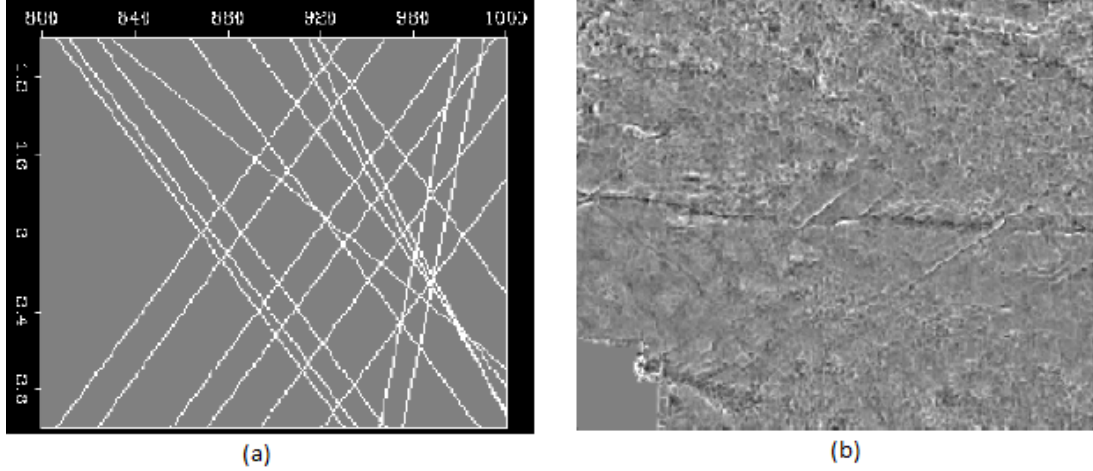


Figure 2.2: (a) The infinite lines produced by the method used in [9], (b) The background noise produced by method in [9].

To solve the problem of infinite lines as shown in Figure 2.2 (a), in which all lines run from the beginning of an edge to the end of another edge and the problem background noise as shown in Figure 2.2 (b), Jacquemin *et al.* [12] employed a double Hough transforms to automatically extract fault line. The first step involves the computation of the semblance based coherence of the seismic data, the resulting coherence section is thresholded, the new image contains binary points corresponding to fault edges and some foot print noise due to acquisition. The second Hough transform is then applied to the binary image to obtain the final parametric space. Each point in the space corresponds to a line in the space of the seismic cube and the pixels are stored in a subset of points.

In order to improve the quality of seismic fault line detection and reduce the effect of noise in the final result of the work in [11] and [12] a semi automatic algorithm was proposed by Wang *et al.* [1] applied to track fault lines in seismic

data using an improved approach of the Hough transform. The approach is an inherently multi-stage one which enhances the likelihood of fault points by obtaining the discontinuity map of the seismic section first. In the second stage, the fault features were detected using the Hough transform. Before that, a double threshold method was used to remove the false features based on certain geological constraints. An initial fault line is then obtained by connecting the remaining fault features.

To improve the efficiency of interpretation and accuracy of fault point detection, the authors in [13] proposed a 3D Hough transform that automatically detects the fault surface. The process involves highlighting possible fault points by calculating the 3D discontinuity map, then a threshold is applied. After that, the 3D Hough transform is applied to the 3D seismic data, in which the seismic space is converted to a sinusoid curve in the parametric space. For fault surface labelling, each plane detected in the seismic space is determined by a group of highlighted fault points and a weighted fitting method with geological constraints is used to delineate the fault. In a continued effort to improve detection of fault points, the authors in [14] used the discontinuity map and the detected lines obtained in [1] to track fault surfaces. To achieve this, a tracking vector is estimated using local windows of particular sizes.

The fault segment is recognised by moving the analysis window. The projected fault line is obtained after the lines are connected. The tracking vector causes displacement between solid lines and discontinuous lines initially detected. A fault

line is generated based on the most discontinuous position between the two projected fault lines. An objective function is used to combine the three fault lines into one fault line. The fault lines in the seismic data are delineated by defining a reference section. The remaining of the seismic section is labelled as predicted sections. These sections are labelled in a two-way projection or prediction. The tracking vector is the vector that connects a fault line in a reference section to the projected fault lines in the predicted section. Another fault line in the discontinuity position is generated and an optimization function is used to combine the three fault lines into one single fault line. The main advantage of using this method is the ability to automatically label fault lines, however, the approach has a draw back of being computationally expensive, and inability to completely filter out noise in the seismic section.

2.1.2 Fault Detection Based on Ant Colony Optimization Algorithms

The fact that seismic attributes are sensitive to noise is undisputable and this often affects the accuracy of the detected fault lines. To address this problem, Basir *et al.* [8] first applied a diffusion filter to the original seismic section in order to enhance the quality of the seismic data. The various seismic attributes sensitive to discontinuity including curvature and similarity were then applied to the 3D data set. The ant colony optimization algorithm is a technique for solving computational problems which can be reduced to finding the best path. An ant

tracking algorithm was applied to track, capture, and improve visualization of the fault features. The authors also applied a artificial neural network to combine the different attributes into a single image that allowed a view of different fault sensitive attributes together.

Yan *et al.* [9] employed the ant colony algorithm to automatically track fault points in a seismic section. The algorithm reduces the level of noise in the coherence cube and improves continuity of the fault line in the cube. The comparison of the algorithm performance and ground truth shows that the algorithm accurately tracks fault points. The first step involves the coherency cube computation. The seismic 2D coherency is decomposed into $M \times N$, and an ant is placed on each block whose position is determined using a certain probability function.

The smaller coherence value corresponds to the probability of being selected as the start point. In order to determine the tracking direction of the ant, an orientation field is calculated where the angle of the orientation field represents the dipping of the faults. Since not all ants are placed in the fault region, an adaptive stopping criterion is employed to put the ant to a halt when moving in the wrong direction, hence, automatically terminating the tracking process. A normal step is recorded if the ant encounters a fault like point while an abnormal step is recorded if the ant encounters a non -fault like point. The ant colony approach has the advantages of reducing noise level and improving discontinuity. However, the major disadvantage is the computational complexity of the algorithm.

2.1.3 Fault Detection Based on Directional Filters

In 2006, Barnes [24] used the facts that faults are usually planar and steeply dipping when compared to other sources that cause discontinuity and developed a filter that consists of three constituent filters that identify the position, orientation and the best fitting of a fault. The fault region of a 3D seismic discontinuity data is distinguished from other regions by passing the data through a small filter. The filter fits them to a plane and verifies if the plane is a fault segment. The filter has the capability to pass discontinuity that is vertical, planar and relatively centred and rejects other sources of discontinuities and also the ability to judge the position, orientation and fit the best fitting plane. A weighted least square fit is used to all the points in the window.

Machado *et al.* [25] proposed a method of improving and enhancing the display of fault images. In their approach, the directional Laplacian of a Gaussian operator is applied to improve the resolution of fault features within a coherence volume. In the first step, a second moment tensor distance-weighted coherence volume is computed within a 3D analysis window about each voxel and is utilized to estimate faults dip and faults azimuth. The orientation of the planar discontinuity is defined by the eigenvectors of the a matrix while the eigenvalues are used to determine the significance of the discontinuity. In the next stage, an edge enhancement technique is used by applying the Laplacian of a Gaussian (LoG) filter to coherence anomalies (changes) along reflector dip and azimuth. The LoG filter is modified to be directional with the short dimension of the operator perpendicular to the

fault position of unconformity anomaly. The technique reveals a high level of robustness when applied to 3D data set.

In [26], Jeong *et al.* used a set of nonlinear filters coupled with a GPU (Graphic Processing Unit) to implement an interactive nonlinear volumetric processing. The seismic orientation is measured using 3D tensors. These tensors serve as a guide to the anisotropic diffusion which lead to noise reduction in the data as well as improving fault discontinuity and coherency along seismic strata. A non-maximal suppression method was employed by the authors to compute the fault likelihood volume using a measure of the directional variance. Finally, the comparison between GPU and central processing unit (CPU) implementation shows that the GPU has a better performance and efficiency. Filtering approaches have a number of advantages; these include noise reduction, fault enhancement, and lower computational cost. However, these approaches do not label fault regions automatically and important informations may be lost due to the use of different filters.

2.1.4 Fault Detection Based on Active Contour

The authors in [27] proposed a semi-automatic fault tracking method for 3D seismic data which is divided mainly into two stages, a fault highlighting stage and a model based fault tracking. The authors replaced the commonly used coherence attribute by the log-Gabor filter for fault highlighting based on the fact that the coherence attribute cannot be obtained with an arbitrary bandwidth without

making the filter output dependent upon the input intensity. In the first stage, a log-Gabor filter which was originally used to model visual cortex cells was used to highlight the fault in order to emphasize the amplitude orientation of fault in the presence of faults. An active contour is then fitted to track the highlighted fault voxels. The active contour identifies smooth and connect curves while ignoring any misleading or missing information. However, the fault tracker requires the active contour to be placed near to a fault on the initial inline by the interpreter. The result obtained in the first inline is then projected to the next inline in order to provide an initial fault pick in this section. Hence, the tracking results on a series of seismic section results to a 3D surface. The method has a drawback of being a semi-automatic method which require human intervention.

2.1.5 Fault Detection Based on Skelotonization

Traditional seismic interpretation uses single channel data for the detection of faults which is mainly based on the contrast between the target region and the background. In an effort to improve fault location accuracy, the authors in [28] proposed a multivariate data map along with colour blending and skeletonization. Three neighbouring time sections viewed in time direction were blended as if they correspond to red, blue and green channels of the colour image. Colour transformation was also applied to extract more reliable structural information. The results suggest that the method shows a high level of accuracy for fault detection by further optimizing the average distance between the fault line and

ground truth data (or labelled data).

Cohen *et al.* [29] presented a novel method for the extraction of fault surface in 3D seismic volumes. The seismic data is converted into a volume of local fault extraction estimates, which represent the likelihood that a particular point lies on the fault surface. The 3D cube is rotated and tilted to identify the fault surface which is partitioned into small regions. The discontinuity associated with the fault surfaces are further enhanced by directional filtering and thresholding. Finally, the local fault extraction estimated volume is skeletonized and the corresponding faults are extracted labelled in order of decreasing sizes.

2.1.6 Other Methods for Fault Detection

Many other authors have used different unconventional methods to detect fault lines. Zhang *et al.* [30] borrowed an idea of biometric algorithm used in detecting capillary vein patterns in human fingers. There are several stages involved in the algorithm, first the coherency volume is transformed into binary form to indicate possible fault points. The binary volume is then skeletonized to produce a set of fault sticks. The last stage involves grouping the fault sticks to construct fault surfaces with the help of classical triangularization method. To minimize the influence of staircase artefact present in the discontinuity volume, the processing stage is applied on a slice by slice.

The authors in [31] developed a computer based methodology that correlates horizons across the faults in 3D seismic data automatically. A geological fault

model is used to obtain the optimal matching point after obtaining seismic feature on both sides of the faults. One side of the fault is assumed to be floating and the other side is assumed to be the reference image. A match is then found between the automatically extracted prominent region on both sides. After that, sparse fault displacement is then computed for this prominent region and the result is used to compute the fault displacement model parameters. Furthermore, simulated annealing optimization scheme was employed to continuously match points.

In [32], Machado and Marcos used a competitive learning algorithm to aid the extraction of fault as a separate object from seismic attributes. The authors argue that even though a lot of seismic attributes have been proposed to measure the discontinuity associated with faults some feature in the attribute maps makes it very difficult to extract fault as a separate object. Competitive learning is a form of neural network that does not require training but extracts the feature from a set of pattern and cluster them into classes. The algorithm consists of two approaches, in the first approach the fault attribute volume is transformed into a graph using a growing neural gas algorithm, this greatly reduces the number of samples to be considered in the surface modelling stage and the graph is then employed to identify the main fault surface. In the second approach, a fault surface triangulation is generated using the Neural mesh algorithm.

Gibson *et al.* [33] discussed fault surface detection in 3D seismic data set. Unlike previous work, the authors attempt to detect several fault line on the same seismic section. The approach is divided into three stages, where in the first stage

they used semblance-based coherence to enhance the fault region. In the second stage, a predefined threshold is applied on the semblance cube. The points with a threshold below a certain value are labelled as a fault. A seed point is obtained by sub-sampling the binary map then grouping these into smaller patches which represent a small section of the fault surface. Finally, the highest confidence first (HCF) merging approach was used to combine the planar patches into a large surface.

2.2 Visual Saliency Models

The original saliency model was introduced by Itti and Koch [34] to represent the attention and shifting focus connected with sight and visual stimuli. A conventional natural scene usually consists of many objects of different structures and spatial scales. The human visual system (HVS) is usually challenged by the complexity of a visual scene. Since there is a large amount of information to be analysed in a given time within its limited capacity, and in order to cope with the vast amount of information, the human visual system has an attention mechanism to select the most important (salient) parts from a scene. The relevant parts of a scene may be selected using two main approaches which are: a bottom-up approach and a top-down approach.

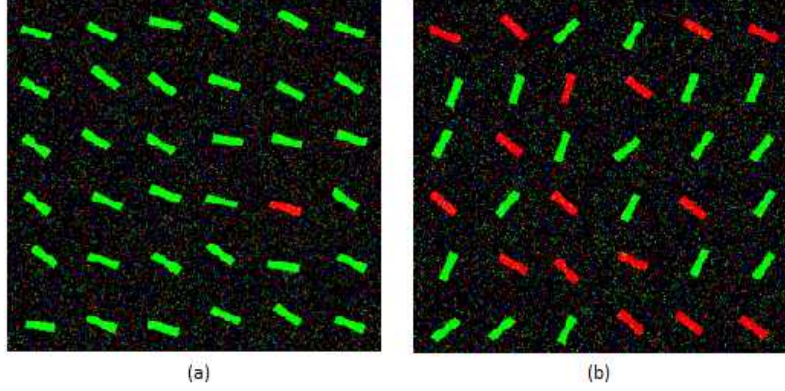


Figure 2.3: (a) Bottom up saliency scenario (b) Top down saliency scenario .

The bottom-up visual attention is usually fast and driven by intrinsic low-level properties of a given scene, in Figure 2.3 (a), one item pops out immediately and effortlessly to attract attention while the top-down attention model involves searching for specific object(s). In Figure 2.3 (b), the unique red bar has to be search by scanning through the image. A real life scenario is illustrated in Figure 2.4. Automatically, our attention is focused on the bicycle parked not the surroundings. Figure 2.4 (a) shows a bicycle as the salient object within an empty surrounding while Figure 2.4 (b) shows a saliency map highlighting the bicycle as the prominent part of the image.

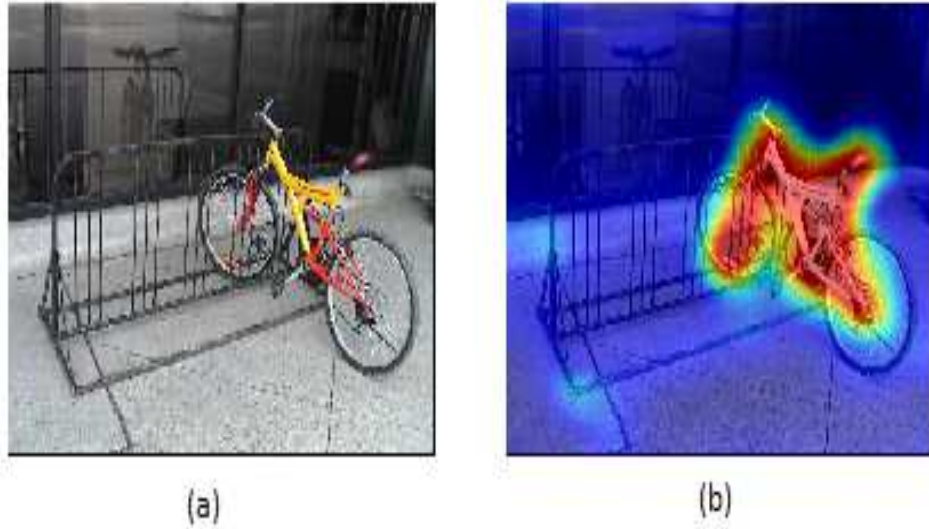


Figure 2.4: (a) A bicycle as the prominent object (b) Saliency map highlighting the bicycle.

Recent years have witnessed a flood of methods for estimating visual saliency. In [34], the authors introduced a biologically inspired saliency model. A set of features from different channels such as colour, intensity, and orientation are used. The final saliency map is obtained by normalizing the obtained feature map from each channel, then applying a linear combination strategy to combine the maps. Although the saliency map is able to predict human fixation successfully, there is no objective function to be optimized and many parameters are tuned manually. The proliferation of eye tracking data has enabled researchers to tackle the problem of human visual attention using different mathematical and statistical methods [35, 36, 37, 38, 39].

The authors in [40] proposed a saliency model that employs the maximum information from an image sample. The saliency model is computed based on

Shannon’s self-information. The probability density function is estimated based on a Gaussian kernel density in a neural circuit.

In [35, 36, 37], a framework for top-down and bottom-up saliency as a classification problem is presented and solved by minimizing the classification error. The framework was initially applied to detect an object in which a set of features are selected such that a class of interest is discriminated from other classes and the resulting weighted sum feature is used to define the saliency of that class.

In [41], the authors used a bottom-up saliency strategy in which a location is seen as salient only if it is distinguishable from its surroundings. They employed the difference of Gaussian filter and the Gabor filter to measure the saliency of a point as the Kullback-Leibler (KL) divergence between the filter response histogram at a point and that of its neighbouring region. In [39], the authors proposed a Bayesian approach for the task of visual saliency that detect salient objects using natural statistics and estimates the probability of target at each location. Visual saliency has been used to solve different problems in computer vision which include object recognition [42], scene classification [43], object tracking [44], video compression [45], image retargeting [46, 47, 48], etc.

2.3 Saliency Estimation

Saliency computation approaches can be grouped into three main groups: the biological approach, the purely computational approach, and a hybrid approach that combines both the biological and the purely computational approaches.

The main aim of any approach is to detect certain properties such as contrast, rarity, unpredictability of a particular region in an image and its surrounding. This could be achieved locally or globally with the aid of certain low-level features extracted from the image such as color, orientation, and intensity. The biological based approach uses the working principle of the human visual system to detect saliency. The purely computational approach achieves the same objective using a different principle such as information theory, signal processing, spectral decomposition and so on. Among these algorithms some use single scale [34, 49] while others use multiple scales [50, 51]. In certain cases, the final saliency map is obtained by separately creating a certain feature map then combining these while in other cases , a saliency map is directly computed from the input image [49] .

2.3.1 Biological Models

In 1987, Koch and Ullman [52] proposed a biological plausible saliency architecture. Later in 1998, Itti *et al.* proposed an algorithm that works based on this technique. In their algorithm, the center surround was computed using the Difference of Gaussian (DoG) approach. Walter and Koch [53] proposed a workflow that was very similar to that of itti *et al.* but with an extension to infer proto objects [54, 55] at a particular location. Han *et al.* [56] and Ko and Nam [57] used a saliency algorithm to segment salient objects. Frintrop *et al.* [58] proposed an algorithm that is similar to the itti's approach but uses the Difference of Boxes (DoB) filter to compute center surroundings, hence speeding up the computation

with integral images.

2.3.2 Purely Computational Models

The purely computational approaches use mainly mathematical or statistical principles for saliency computations. Zhang *et al.* [59] proposed two different methods of computing bottom-up saliency, each of these methods uses different feature sets. One of the methods uses independent component analysis (ICA) obtained from machine learning similar to Bruce and Tsotsos workflow while the other method uses four scales over color and luminance.

Mahadevan and Vasconcelos [60] used the bottom-up approach to subtract background in a highly dynamic scene. Ma and Zhang [50] calculated the location of its surrounding region as a cumulative sum of color distances of the center region with surround regions. Statistical fuzzy growing was applied to the saliency map to place segment rectangular boxes that contain the salient regions.

Achanta *et al.* defy the use of the famous Difference of Gaussian filter and used center surround feature distance and a DoB approach with the integral image like Frintrop *et al.* The work is computationally efficient despite the full resolution image filtering performed. Hu *et al.* [51] estimated saliency by first using histogram thresholding of feature maps and then applying a heuristic measure.

Seo and Milanfar, proposed the estimation of saliency in images and videos by measuring the similarity of feature descriptors in a particular location with the surrounding descriptors. Rosin [61] applied an edge scheme to compute the

saliency for gray scale images. A Sobel operator is used to perform edge detection on the input image. A binary image is obtained by thresholding the gray level gradient map. A distance transform is then applied to propagate edge information. An average of the resulting output is taken to produce the saliency map. Finally, a binary threshold algorithm is employed to extract the saliency map. Hou and Zhang [62] estimated saliency using a spectral domain approach. The saliency was computed by taking the difference perceived and characteristic spectrum. Guo *et al*, used the inverse transform of phase spectrum to get the equivalent result. The method was later simplified by Zhang [57].

This idea of saliency has rarely been used in seismic image processing for fault tracking or detection, however, in [58], the authors used saliency to track the horizon in seismic image, the authors divided the work into several steps, first, the Shannon entropy and the generalized entropy was computed at each of the pixel locations within a neighbourhood. Then, the variable and fixed scale difference between the two entropies was obtained and the saliency measure was then computed for both cases. Experimental results demonstrated that the algorithm was better adapted for horizon tracking in the seismic sections.

The authors also compared the results obtained by using Shannon entropy and the Generalized Cumulative Residual Entropy (GCRE). The authors concluded that, while, Shannon entropy gave a better result for the detection of both secondary reflectors and lateral continuity, the GCRE is more adapted for the detection of the strong reflectors and has a better physical sense as a result of

its scale property. Salient features for describing and analysing local textures complexity were computed for both entropy measures. Finally, the authors suggest that both approaches can be applied to other image attributes, for example, instantaneous frequency and instantaneous phase and other geometric attributes like dip, azimuth, curvature, coherence to detect salient feature like a fault.

2.3.3 Hybrid Models

This approach combined the ideas that are partly based on computational and biological models. Harel *et al.* [63] proposed a method that produces feature maps using Itti's approach but applies the graphical model to normalize the maps. Also Bian and Zhang [64] explain the biological rationale behind their method. Torralba *et al.* [65] used natural image statistics and global scene context respectively. The authors explained the biological plausibility of their methods. In this work, we used the computational approach to develop a saliency model that automatically recognises fault region in seismic data set. The model employs different seismic attributes capable of enhancing fault regions in seismic dataset such that fault becomes the region of interest. The next Chapter explains the various seismic attribute we used.

CHAPTER 3

SEISMIC ATTRIBUTES

Seismic attributes can be seen as the different characteristic features of seismic data which are obtained by computation, measurement, or other methods [66]. These help in visually enhancing or quantifying features of interest useful in interpretation. A good seismic attribute should be visually sensitive to the desired geological features or reservoir properties of interest. This enables the interpreters to infer additional desired information. Seismic attributes were introduced in early 1970's as part of seismic interpretation [66]. Since then, many new attributes were derived and computed.

These attributes are very vital in seismic interpretation because of their ability to enhance subtle features that in turn provide an easier seismic section ready for human interpretation. The main aim of seismic attributes is to quantify the amplitude and other morphological features recognised in the seismic data using scientific calculation and mathematical models. It is important to note that the quality of the data and the robustness of the workflow impact substantially the

performance of overall seismic data analysis and the final interpretation results. Poor signal quality, low-frequency content, and improper processing, all hinder the amount of information derived or extracted from a given set of attributes.

Seismic attributes can be classified into two groups, [67] these are: physical attributes and geometric attributes. Physical attributes are defined as the attributes that are related directly to lithology and wave propagation. The physical attributes are classified further into post-stack and pre-stack attributes. Each of these has sub-classes such as instantaneous and wavelet attributes. Instantaneous attributes are attributes that change continuously along the time and space axes and are usually computed sample by sample. On the other hand, the wavelet attributes represent frequency characteristics of data.

The popular geometrical attributes include dip, azimuth, and discontinuity. The dip attribute is useful in making faults more prominent. Discontinuity attributes measure the lateral relations in the data. They are designed to enhance the discontinuous regions such as faults in seismic sections. High amplitude values of this attribute correspond to discontinuities in the data while low amplitude values correspond to continuous events. In this work, we will consider mainly four attributes that highlight fault regions these include variance-based coherence, curvature, dips and gradients because of their sensitivity to fault regions in seismic data set. In this chapter, we will discuss the various types of attributes that enhance faults or discontinuity regions. Figure 3.1 (a)-(c) shows inline 256, inline 272 and inline 249 respectively obtained from Netherlands offshore, F3 block (the

dataset is discussed in more detail in Section 1.6), different attributes that are sensitive to discontinuous regions or faults will be calculated on this sections.

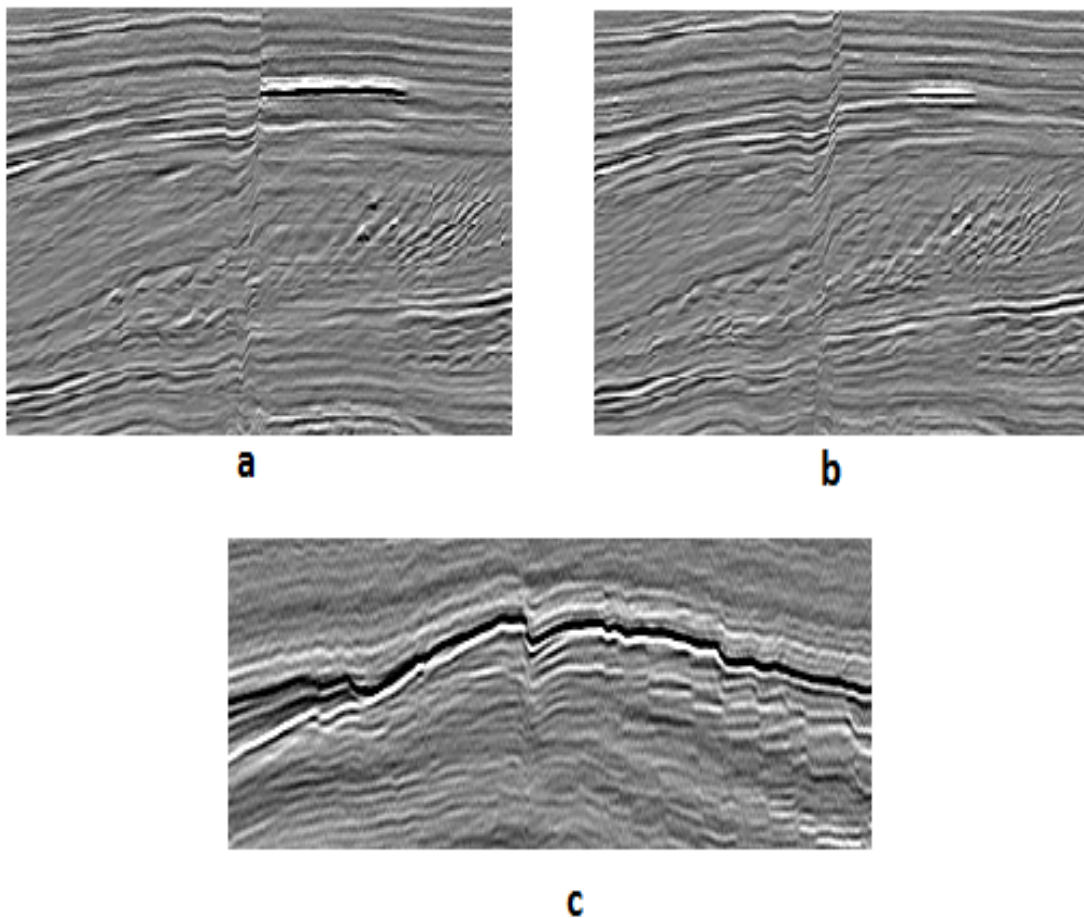


Figure 3.1: (a) Inline 257 (b) Inline 272 and (c) Inline 249 from the F3 dataset.

3.1 Coherence Attribute

Coherency is the similarity between wave form. The coherence attribute was introduced by Boharich and Farmer in 1995, a cross-correlation technique was used to compute the coherence coefficient from the seismic amplitudes of adjacent traces [16]. A more accurate and coherence computation was later developed based

on semblance [17] and later the eigenstructure [18] better than cross-correlation based. The resulting coherence image reveals clearly buried deltas, river channel, reefs, fractures, and faults. The way in which the detail stratigraphic features shows up is remarkable when compared to the original seismic slice.

There several advantages of using the coherence based attribute in the literature some of which are, the coherence slice provides a platform for viewing faults that are parallel to strikes that are difficult to recognise in an a typical time slice, it reveals fault in any orientation , the relationship between structure, stratigraphy and hydrocarbon are also very visible in the coherence slices, edge detection techniques can also be applied to enhance the coherence slice features, it distinguishes clearly between fault region and neighbouring data and makes them numerically separable

Among the several types of coherency. Here, we discuss cross-correlation-based coherency, semblance-based coherency, least squares-based coherency, variance-based coherency and eigen structure-based coherency. The computations will also take into account the local dip and azimuth of the reflector to avoid low coherency artefacts that reflect structure anomalies of interest. The following are some of the coherency based computations

3.1.1 Semblance-based Coherence

Semblance based coherency can be defined as the measure of the level of similarity among the traces along a predefined dip and within the rectangular or elliptical

analysis window.

It has a lot of advantage over the three trace cross-correlation coherence among which is improved vertical resolution, it allows for less quality data to be analysed, it decreases mixture of overlaying and underlying stratigraphic features, it accelerates the interpretation process, identifying and interprets subtle features that are not representable by picks or peaks, and generates paleo-environmental maps of channel and fans [17]. The semblance based coherence $c_s(t, p, q)$ of a group of traces u_j at time t with apparent dips p and q is given in equation 3.1. Figure 3.2(a)-(c) show the semblance map for inline 256, inline 272 and inline 249 respectively, the prominent fault regions in each of the inlines is clearly highlighted with noise around it, the fault regions have lower coherence value while the non fault regions have a higher value.

$$c_s(t, p, q) = \frac{\sum_{k=-K}^K [\frac{1}{J} \sum_{j=1}^J u_j(t + k\Delta t - px_j - qy_j)]^2}{\sum_{k=-K}^K \frac{1}{J} \sum_{j=1}^J [u_j(t + k\Delta t - px_j - qy_j)]} \quad (3.1)$$

where, j is the j th trace that is within the analysis window, x_j and y_j are the x and y j th trace distances from the centre of the analysis window, K is the analysis window length, u_i is the intensity at point x_j and y_j . p and q are the apparent dips measured in milliseconds per meter or per foot which define a local planar event at time t , and Δt is the sampling time.

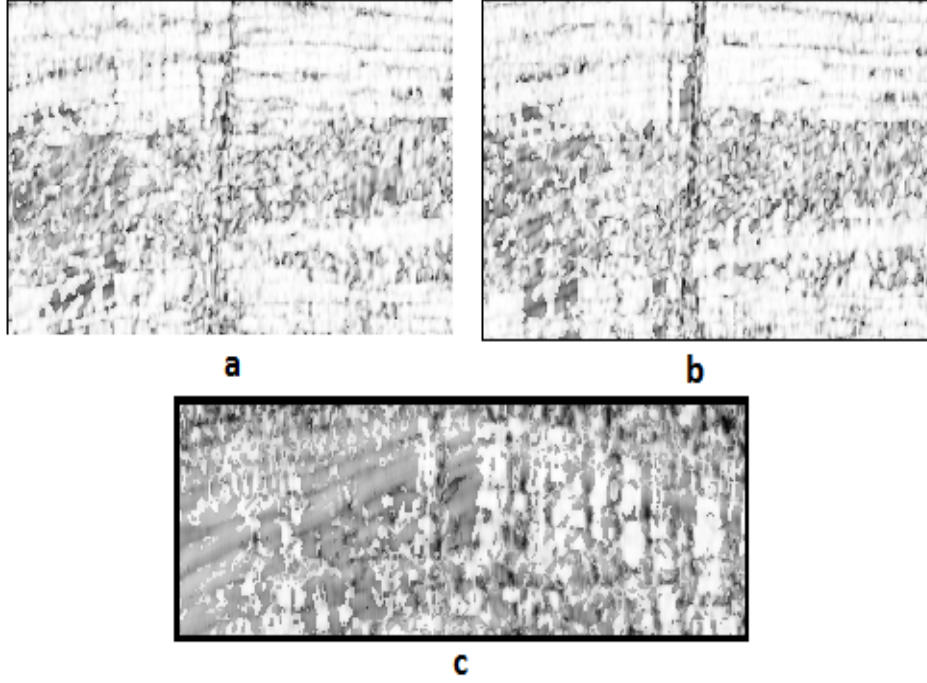


Figure 3.2: The semblance based coherence of (a) inline 256 (b) inline 272 (c) inline 249.

3.1.2 Variance-based Coherence

The variance based coherence is also a very useful attribute, it is identical and has similar advantages to the semblance-based coherence explained above. It is obtained by modifying the formal definition of variance. The variance based coherence $c_v(t, p, q)$ of a group of traces u_j at time t with apparent dips p and q is given in equation 3.2. Figure 3.3 (a)-(b) shows the variance based coherence map of inline 256, inline 272 and inline 249 respectively, it behaves similarly to the semblance based coherence, however the fault region in this case has higher pixel value than the non fault region.

$$c_v(t, p, q) = 1 - \frac{\sum_{k=-K}^K [\frac{1}{J} \sum_{j=1}^J u_j(t + k\Delta t - px_j - qy_j)]^2}{\sum_{k=-K}^K \frac{1}{J} \sum_{j=1}^J [u_j(t + k\Delta t - px_j - qy_j)]} \quad (3.2)$$

where $c_v(t, p, q)$ is the variance based coherence, j is the j th trace that is within the analysis window, x_j and y_j are the x and y j th trace distances from the centre of the analysis window, K is the analysis window length, u_i is the intensity at point x_j and y_j . p and q are the apparent dips measured in milliseconds per meter or per foot which define a local planar event at time t and Δt is the sampling time.

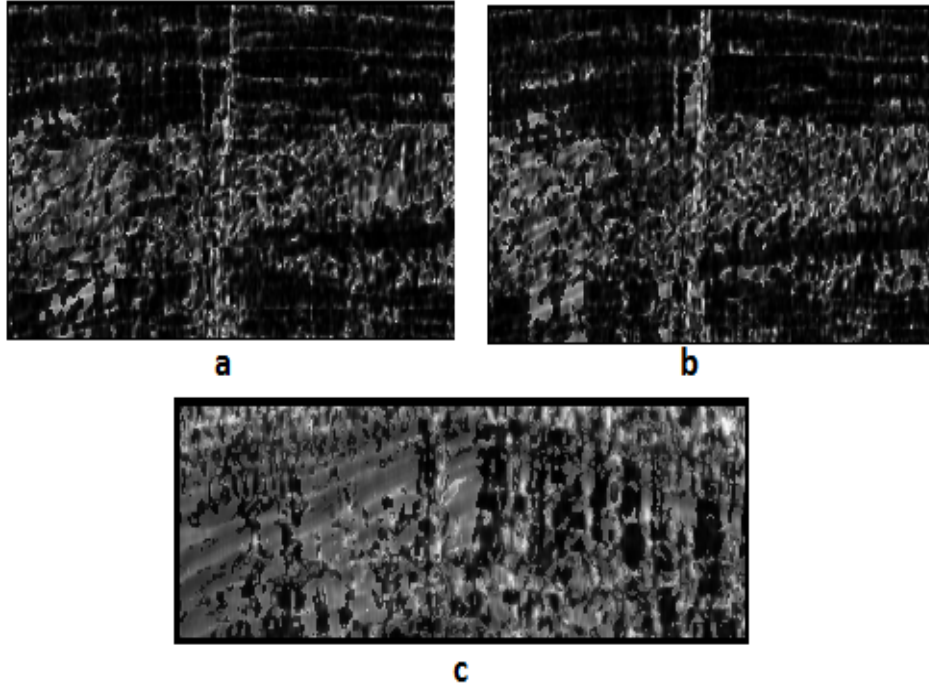


Figure 3.3: The variance based coherence of (a) inline 256 (b) inline 272 (c) inline 249.

3.1.3 Eigenstructure-based Coherence

The Eigenstructure based coherence address the drawbacks of the semblance and variance based coherence of being sensitive to waveform and lateral changes amplitude of seismic waves. The eigenstructure coherence is the ratio of a coherent component of the data to the original seismic trace energy. Assuming that \mathbf{C} is the covariance matrix of the data traces and λ_1 is the largest of the eigenvalues λ_j , J is the total number of eigenvalues obtained from the covariance matrix, then the estimate of the eigenstructure coherence E_c is given as

$$\mathbf{C} = \mathbf{U}\mathbf{\Lambda}\mathbf{U}^{-1} \quad (3.3)$$

where \mathbf{U} is the matrix whose i^{th} column is the eigen vector u_i of \mathbf{C} and $\mathbf{\Lambda} = diag(\lambda_1, \dots, \lambda_J)$ is the diagonal whose element are the corresponding eigenvalues.

$$E_c = \frac{\lambda_1}{\sum_{j=1}^J \lambda_j} \quad (3.4)$$

Figure 3.4(a)-(c) shows the Eigenstructure coherence based map of inline 256, inline 272 and inline 249 respectively. In this case, the fault regions are darker than the other region with lower coherence value while the non fault regions have higher coherence value but less noisy relative to the semblance and variance based coherence.

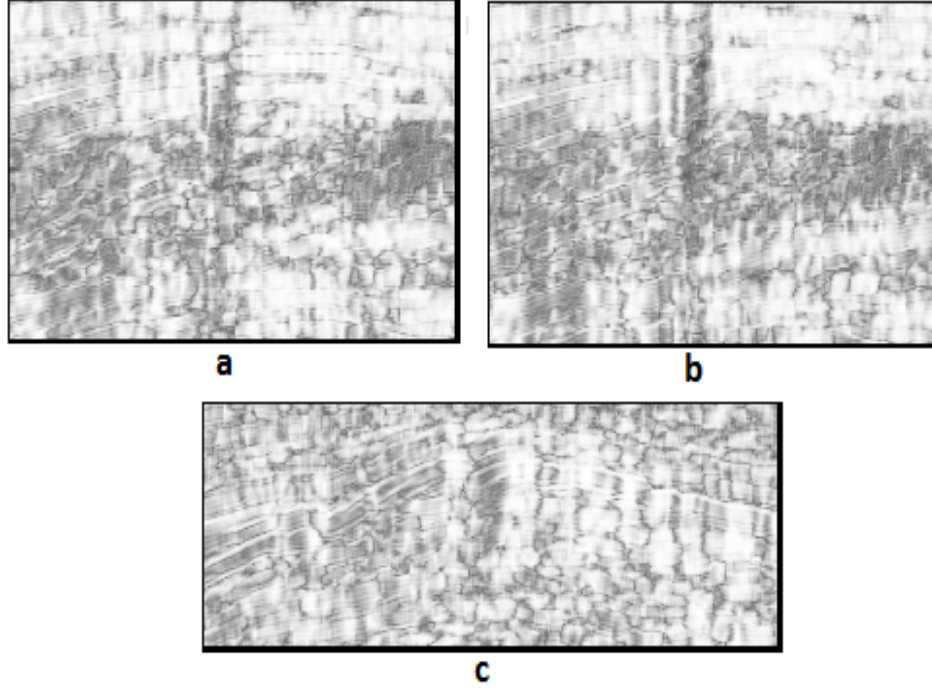


Figure 3.4: The eigenstructure based coherence of (a) inline 256 (b) inline 272 (c) inline 249.

3.2 Curvature Attributes

The curvature is a two-dimensional property of a curve that describes how bent a curve is at a given point on the curve i.e it quantifies the extend at which curve deviates from a straight line. For any given point on a curve, its curvature can be described as the rate of change of the curve. In 1994, Lisle demonstrates the relationship between curvature measure (Gaussian) with open fracture measure on outcrops [68].

A significant improvement has been made in using curvature as an attribute by using multispectral volumetric computational approaches [23] . It's main purpose

is to enhance certain properties of a surface that may be very difficult to observe directly such as fractures, flexures, and folds. For a given seismic section with a crossline x and inline y directions respectively, the curvature K at any point is the reciprocal of the radius of curvature and can be expressed in terms of derivatives.

$$K = \frac{\frac{d^2y}{dx^2}}{(1 + (\frac{d^2y}{dx^2})^2)^{\frac{3}{2}}} \quad (3.5)$$

for more detail explanation on curvature refer to [68].

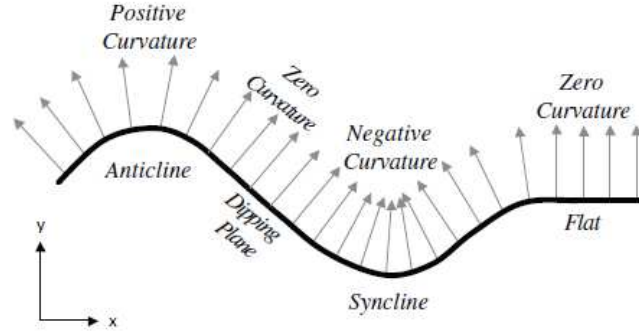


Figure 3.5: 2D illustration of curvature at different point in a surface.

3.3 Curvature in 2D Cross-Sections

The curvature can be viewed in 2D cross section as shown in Figure 3.5. The vectors normal to the plane along the horizon are distributed in grey at regular interval. A flat and planar dipping horizon correspond to parallel vectors. Therefore, these region has zero curvature. An anticline or ridge feature corresponds to diverging vectors and the curvature of this region is known as positive curvature. A syncline corresponds to a converging vectors called the negative curvature. Dif-

ferent curvature are formed as a result of different orientations cross section. This concept can be easily extended to 3D. The curvature in the crossline, x and depth y direction can be calculated by fitting a polynomial in a grid cells say $N \times N$, the calculation of the coefficient simplifies a series of arithmetic expression following expression [68].

$$z(x, y) = ax^2 + by^2 + cxy + dx + ey + f \quad (3.6)$$

where x is the cross line and y is the depth directions, a, b, c, d, e , and f are the coefficient of the fitted grid polynomial. Several curvature attributes can be obtained from the coefficient of the equation (3.6). These include the mean curvature, Gaussian curvature, maximum curvature, minimum curvature, most positive curvature, most negative curvature, dip curvature, strike curvature and contour curvature. However, the most positive and most negative are the most useful in that they are closely related to a typical interpretational workflow. Some curvature properties like shape index, contour and curvedness will also be explained below

3.3.1 Most Positive and Most Negative Curvature

The maximum curvature attributes contain large amount of information that may be sometimes confusing. An edge type display can be derived from the normal curvature, for the most positive and most negative. The resulting attribute is called most positive curvature K_+ and most negative curvature K_- [68]. In both

cases, the fault region is well highlighted, Figure 3.6 (a)-(c) shows the most positive curvature of inline 256, 272 and 249, Figure 3.7 (a)-(c) shows the most negative curvature of inline 256, 272 and 249, in both cases, the detail information of the fault regions were displayed when compared with the coherence.

$$K_+ = (a + b) + \sqrt{((a - b)^2 + c^2)} \quad (3.7)$$

$$K_- = (a + b) - \sqrt{((a - b)^2 + c^2)} \quad (3.8)$$

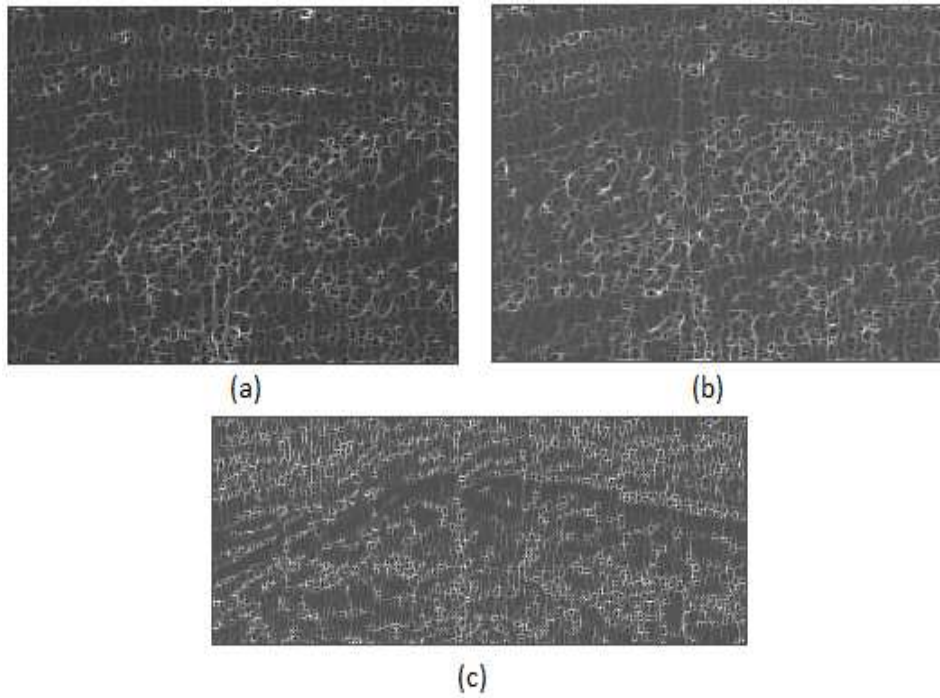


Figure 3.6: The most positive curvature attribute of (a) inline 256 (b) inline 272 (c) inline 249.

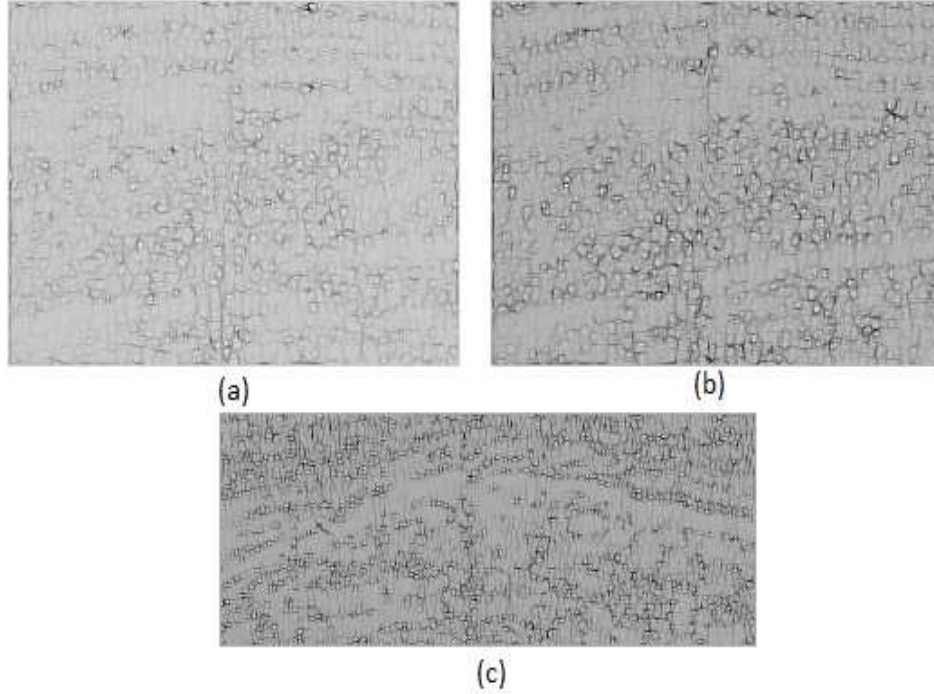


Figure 3.7: The most negative curvature of (a) inline 256 (b) inline 272 (c) inline 249.

3.4 Dip Attribute

The dip attribute originally described by Dally *et al.* The authors mention that the dip along with shaded relief can highlight subtle faults as well as stratigraphic features that manifest itself through differential compaction or through changes [69]. In 1991, the authors of [70] show that horizon-based dip magnitude and dip azimuth are effective in delineating subtle fault which is a fraction of seismic wavelet. An experience interpreter recognises alignments of such subtle offset in map view as being either faults or artefacts. Just like the coherence, there are several ways of computing the dip and azimuth from seismic data which includes

aligning the phase derived from complex trace analysis, discretely scanning for the most coherent reflector and cross-correlating the gradient of the data and forming a gradient structure tensor.

The first method for computing dips is based on complex analysis will be considered in this work. The authors of [20] described the method of computing vector dip based on a 3D extension of the complex trace attributes. For details on complex trace analysis, the reader can refer to [71, 20]. For a given seismic data u with inline direction x and crossline direction y , and to calculate the dip, we first calculate the instantaneous wave numbers $K_x(x, y)$ and $K_y(x, y)$.

$$K_x(x, y) = \frac{u \frac{du^H}{dx} - u^H \frac{du}{dx}}{(u)^2 + (u^H)^2} \quad (3.9)$$

$$K_y(x, y) = \frac{u \frac{du^H}{dy} - u^H \frac{du}{dy}}{(u)^2 + (u^H)^2} \quad (3.10)$$

where u is the input seismic data, H is the Hilbert operator, and u^H is the Hilbert transform of the 2D seismic data. If the input is in depth domain rather than in time domain, we calculate $K_z(x, y)$ as:

$$K_z(z, x, y) = \frac{u \frac{du^H}{dz} - u^H \frac{du}{dz}}{(u)^2 + (u^H)^2} \quad (3.11)$$

The instantaneous dips is then obtained as follows

$$\theta_x = \tan^{-1} \frac{K_x}{K_z} \quad (3.12)$$

$$\theta_y = \tan^{-1} \frac{K_y}{K_z} \quad (3.13)$$

$$\theta = \tan^{-1} \frac{(K_x^2 + K_y^2)^{\frac{1}{2}}}{K_z} \quad (3.14)$$

where θ_x and θ_y are the instantaneous dip and θ is the dip. Figure 3.8 (a)-(c) shows the dip attribute map for inlines 256, 272 and 249, respectively, in this case the dip focus mainly on the mild and subtle fault, the mild fault regions are darker compared to the other region.

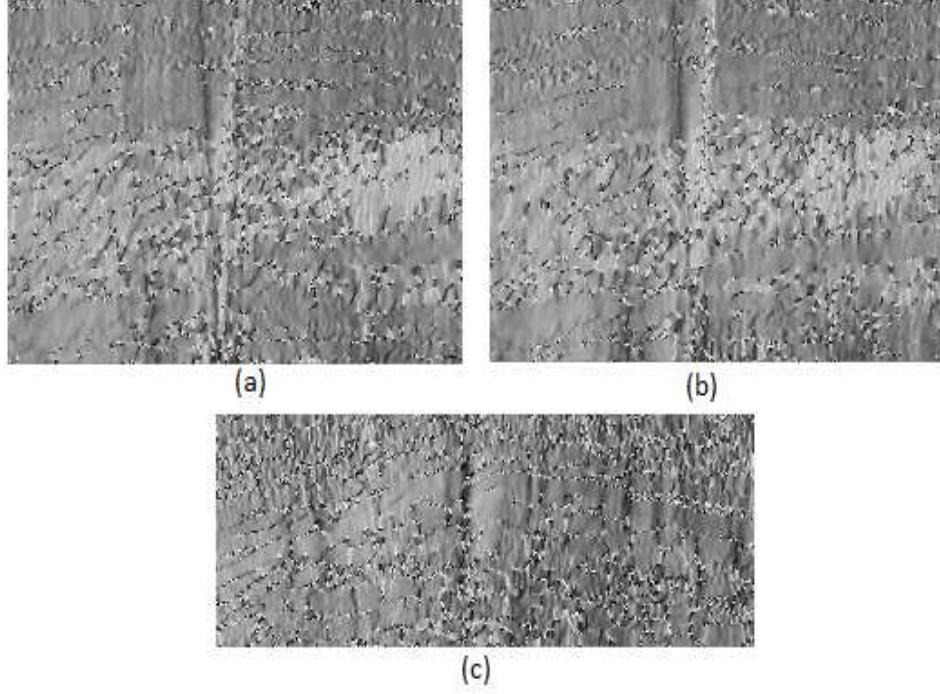


Figure 3.8: The dip of (a) inline 256 (b) inline 272 (c) inline 249.

3.4.1 Weighted Dip

In [15], a weighted average dip attribute was proposed in order to filter out the noise content in the original seismic attribute. For detail, the reader can refer to [15]. This is obtained by weighting the dip with the amplitude of the original seismic data. The result is shown Figure 3.9 (a)-(c) displaying the dip of inlines 256, 272 and 24, respectively, in this case the noise performance of the algorithm has greatly improved.

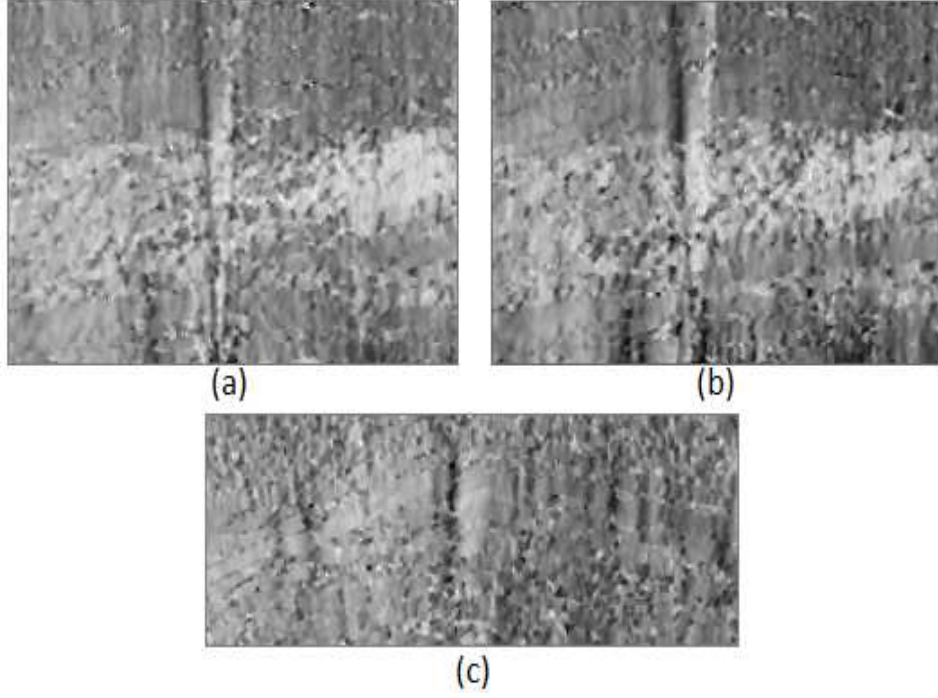


Figure 3.9: The weighted dip of (a) inline 256 (b) inline 272 (c) inline 249.

3.5 Gradient Attribute

The gradient is very important as it highlights edge information. Here, we compute the gradients in the x -direction and in the y -direction which correspond to the cross line and the depth, respectively. However, here, we consider the gradient in the x -direction as it enhances the fault region more prominently.

$$\frac{du(x, y)}{dx} = \frac{u(x + \Delta x, y) - u(x, y)}{\Delta x} \quad (3.15)$$

$$\frac{du(x, y)}{dy} = \frac{u(x, y + \Delta y) - u(x, y)}{\Delta y} \quad (3.16)$$

where $\frac{du(x,y)}{dx}$ and $\frac{du(x,y)}{dy}$ are the gradients in the x and y directions, respectively corresponding to the cross line and depth directions of the seismic section. The gradient attribute of inlines 256, 272 and 249, is shown in Figure 3.10 the edge information which corresponds the fault regions are clearly highlighted.

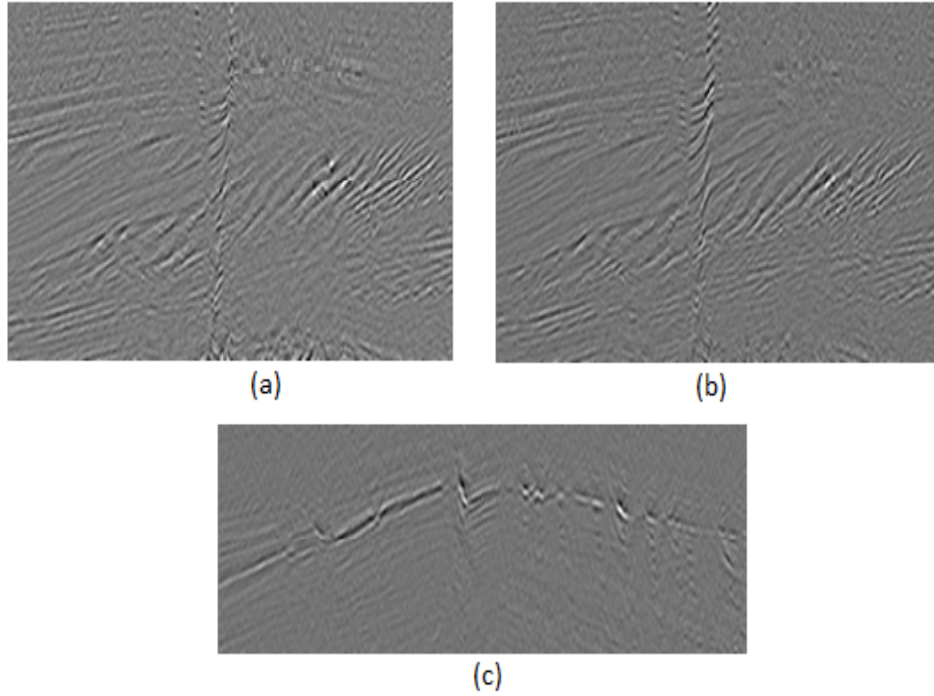


Figure 3.10: The gradient of (a) inline 256 (b) inline 272 (c) inline 249.

3.6 Other Fault Enhancing Attributes

There are other fault enhancing attributes such as the maximum and minimum curvature, they are quite effective in delimiting faults and faults geometry. These can also be seen as a juxtaposition (placed close together with contrasting effect) of positive and negative curvature values. The dip curvature can be used to enhance compact features, the strike curvature divides the surface into areas of ridges and

valley shapes. The discontinuity map is another useful attribute that enhances fault regions. It is very similar to the variance based coherence attribute. It gives higher values in the discontinuity region and lower values for horizons.

CHAPTER 4

A SALIENCY-BASED MODEL FOR FAULT DETECTION

In this Chapter, we propose a new bottom-up saliency-based approach for fault detection. Here, we propose to use a combination of seismic attributes including coherence, curvature, dip, and gradient in parallel. First, we compute four different seismic attributes, aforementioned, as explained in the previous chapter. In the second stage, we compute the saliency map for each attribute and combine these using empirical weights determined according to the significance of the attributes in highlighting faults. This forms a consolidated saliency map which effectively highlights the fault regions. The saliency map was computed using region covariance as it serves as a low dimensional representation of seismic image patches and captures local image structure better than standard linear filters [72].

In the last stage, which will be explained in Chapter 5, we label faults by thresholding the variance-based saliency map and discuss our approach for con-

necting the binary points. We optimize the fault labels using both the curvature and the coherence maps. The estimated points are optimized to label the fault points by employing curve fitting.

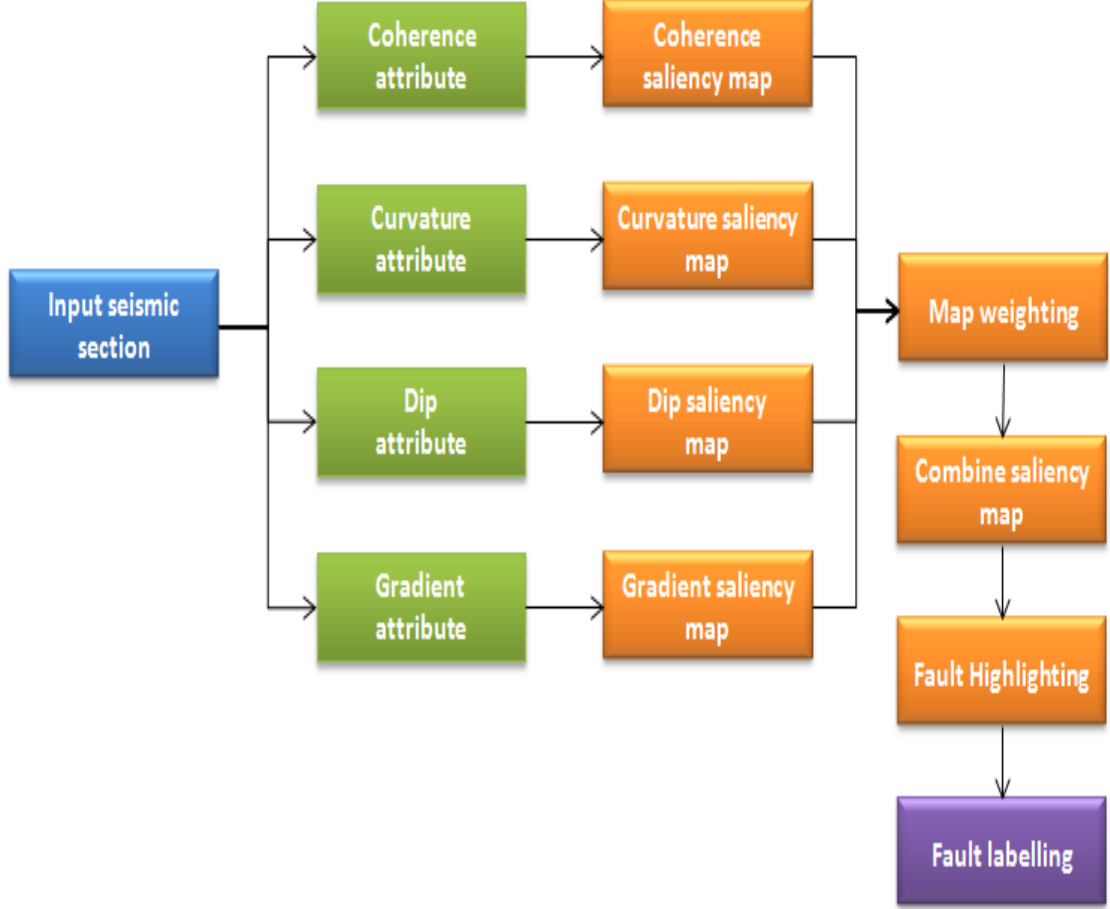


Figure 4.1: Block diagram of the proposed workflow.

4.1 Proposed Fault Detection Model

The overall block diagram of the proposed system is displayed in Figure 4.1. In the proposed method, to detect salient fault regions in seismic sections, first, four seismic attributes namely coherence, curvature, dips, and gradient are computed.

Each of these attributes is normalized to form a grey scale image. The four grey scale images are converted into colour space by replication on the red, green, and blue colour planes. Next, several features such as colour orientation and spatial features are extracted from each attribute to form a multidimensional meta feature vector. Then, the saliency of each attribute map is obtained using the region covariance approach. Each of the steps is now explained in more details.

4.2 Covariance Matrix for The Meta Feature

For a given seismic section, several attributes that enhance fault region including coherence, curvature, dip and gradient, are computed. Each of these attributes is normalized to form a grey scale image. The grey scale images are converted to colour space by replication in the red, green, and blue colour plane, for more implementation detail refer to [73]. The RGB image is rescaled to 512 by 512 to form a square image, after that, the rescaled image is converted to Lab color space to obtain: the Lab components, the spatial direction information in both the x and y directions, and finally x and y positions. Hence, a seven-dimensional feature vector is formed which we call meta feature vector. To estimate the saliency map, the image is converted into non overlapping squares with a scale $k=[16, 32, 64]$. The covariance matrix of each square block is first computed. Then, the regions with nearly the same properties have similar covariance matrices while the dissimilar regions have different matrices. The saliency of the local image patches is computed directly by means of distance between its covariance descriptor and

those of the surrounding patches (see Section 4.5).

It is important to note that incorporating higher order statistics into saliency estimation has also been previously investigated by a number of researchers. Rosenholtz *et al.* in 1999 and 2000 [74, 75] proposed the computation of salient regions or points as the Mahalanobis distance between its features and the mean surrounding features and also taking the covariance of the surrounding feature vector into account. Similarly, Torralba *et al.* in 2003 and 2006 [76, 65] suggested a bottom-up saliency based approach by modelling the local feature distribution with a Gaussian distribution.

4.3 Feature Integration using Region Covariance

The method uses a local description of saliency in which the saliency of a given pixel is measured by how much it differs from its surrounding pixels. This is achieved on a patch-by-patches basis. Each patch region is compared to its nearby surroundings and is represented by its regional covariance descriptor which automatically provides a non-linear feature integration .

4.4 Region Covariance

In 2006, Tuzel *et al.* proposed the covariance of features as a compact region descriptor, since then it has been used effectively in different high-level computer

vision problems including texture discrimination [65], object detection [77], and object tracking. After obtaining the attribute colour image, I , a d -dimensional feature vector is extracted (as explained in Section 4.2) and denoted as F at position (x,y)

$$F(x, y) = \Phi(I, x, y) \quad (4.1)$$

where Φ denote the d - dimensional function of features, x and y denotes the crossline and depth direction respectively. A region R inside F can be denoted with a $d \times d$ covariance matrix \mathbf{C}_R of the feature points

$$\mathbf{C}_R = \frac{1}{(n-1)} \sum_{i=1}^n (\mathbf{f}_i - \boldsymbol{\mu})(\mathbf{f}_i - \boldsymbol{\mu})^T \quad (4.2)$$

where $[\mathbf{f}_i]_{i=1,2,\dots,n}$ denotes the d -dimensional feature points inside R , and $\boldsymbol{\mu}$ is the mean of these points. Tuzel *et al.* [77] suggested an efficient way to compute covariance matrices of rectangular region using integral image representation [78] with $O(d^2)$ computational complexity. It is vital to note that the covariance matrices do not lie on the Euclidean space. Therefore, the distance between any two covariances, say \mathbf{C}_1 , and \mathbf{C}_2 , is computed using the metric discussed in [79] .

$$\rho(\mathbf{C}_1, \mathbf{C}_2) = \sqrt{\sum_{i=1}^n \ln^2 \lambda_i(\mathbf{C}_1, \mathbf{C}_2)} \quad (4.3)$$

$$\lambda_i \mathbf{C}_1 \mathbf{x}_i - \mathbf{C}_2 \mathbf{x}_i = 0, i = 1, \dots, d \quad (4.4)$$

where $\lambda_i(\mathbf{C}_1, \mathbf{C}_2)$ and \mathbf{x}_i are the generalized Eigen-values and generalized Eigen-vectors of \mathbf{C}_1 and \mathbf{C}_2 respectively, which satisfies equation 4.4.

A covariance matrix provides an important way for combining various visual features with the diagonal elements corresponding to the features variance and the non-diagonal elements representing the correlations among the features.

4.5 Local Saliency Estimation

For a given seismic section, after obtaining the colour space attribute image I , we reshape it into a square form, and then decompose it into non-overlapping square blocks of size $k \times k$ pixels as illustrated in Figure 4.2. The saliency of each block is measured by comparing it with its neighbours and its regarded as salient when it displays distinct characteristics. The block properties depend on the pixels within the region, thus the region size, k , determines the scale at which the saliency map generation is performed.

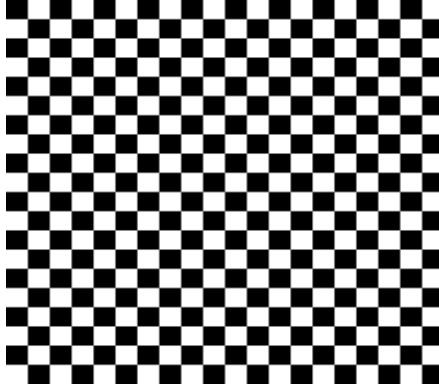


Figure 4.2: A synthetic image illustrating the non overlapping block decomposition.

4.6 The Saliency Model

The saliency model is based on the method discussed in [72], assume \mathbf{R}_i is the region under consideration and whose closest neighbour is defined by the region \mathbf{R}_j with a radius of r . The saliency of \mathbf{R}_i , is the weighted average of the dissimilarity between \mathbf{R}_i , to the m , most similar regions around it. m is chosen to be 1/10 of the number of surrounding regions defined by r . More formally, the saliency of region \mathbf{R}_i is given by

$$S(\mathbf{R}_i) = \frac{1}{m} \sum_{j=1}^m d(\mathbf{R}_i, \mathbf{R}_j) \quad (4.5)$$

The saliency map is computed for each of the seismic attributes and combined to

form a consolidated saliency map, which is given below

$$S_c(\mathbf{R}_i) = w_1 S_{vc}(\mathbf{R}_i) + w_2 S_{cv}(\mathbf{R}_i) + w_3 S_{dp}(\mathbf{R}_i) + w_4 S_{gd}(\mathbf{R}_i) \quad (4.6)$$

where $S_c(\mathbf{R}_i)$ is the combined saliency map, $S_{vc}(\mathbf{R}_i)$ is the saliency map of the variance based coherence, $S_{cv}(\mathbf{R}_i)$ is the saliency map of the curvature attribute, $S_{dp}(\mathbf{R}_i)$ is the saliency map of the dip attribute, and $S_{gd}(\mathbf{R}_i)$ is the saliency map of the gradient attribute, and w_1, w_2, w_3 and w_4 are the respective weights of the different maps. In our work, the weights were selected empirically based on the significance of the attribute in fault enhancement as follows $w_1=0.1, w_2=1, w_3=0.1$ and $w_4=1$. The weights were selected to reduce the spreading effect of the coherence and dip map in a way that only the fault region becomes prominent. It was gradually lowered from 1 until an appropriate value of 0.1 was obtained. The weight of the gradient and curvature was left as 1 because of the lesser spreading effect. The m most similar regions to \mathbf{R}_i can be computed based on the dissimilarity measure $d(\mathbf{R}_i, \mathbf{R}_j)$ defined as

$$d(R_i, R_j) = \frac{\rho(\mathbf{C}_i, \mathbf{C}_j)}{(1 + ||\mathbf{x}_i - \mathbf{x}_j||)} \quad (4.7)$$

where \mathbf{C}_i and \mathbf{C}_j denotes the covariance matrices under consideration and \mathbf{x}_i and \mathbf{x}_j represent the image coordinates of the centres of the regions \mathbf{R}_i and \mathbf{R}_j respectively. In order to determine the distinctiveness of a region, weighting covariance distances by the inverse spatial distance decreases the influences of visual similar

regions and introduces a grouping-like effect.

4.7 Implementation details

The 3D seismic data used in our experiments was obtained from the Netherlands offshore (North sea) F3 block [7]. In our experiments, we considered as a sample image inline 256, to test the robustness of our algorithm. We applied the algorithm on inline 272 with the same parameters, and to demonstrate the performance of the proposed algorithm on multiple faults we applied it to inline 249. First, we computed the attributes of the seismic inlines which include coherence, curvature, dips, and gradient as explained in Chapter 3. The attributes were chosen because of their relevance to faults. Each attribute map was normalized to form a grey scale image and then converted from grey scale image to color space, the image intensity is obtained by taking the average of the RGB images, the intensity is then used to obtain the spatial information in the crossline x and depth y directions. The pixel position were also extracted. Finally, the image was converted to the Lab colour space to obtain the Lab features.

$$F(x, y) = \left[L(x, y), a(x, y), b(x, y), \frac{dI(x, y)}{dx}, \frac{dI(x, y)}{dy}, x, y \right] \quad (4.8)$$

where $L(x, y)$, $a(x, y)$, $b(x, y)$, correspond to the color in the Lab space and $\frac{dI(x, y)}{dx}$, $\frac{dI(x, y)}{dy}$ are the orientations in the x and y directions, respectively. The saliency map was then computed as follows. There are three parameters related to the

notion of the scale

- a. the set of region size, k
- b. neighborhood radius, r
- c. smoothing parameter, σ

The number of most similar neighbors, m is another parameter that needs to be considered. The input image $w \times h$ is rescaled into 512×512 pixels. The product of the saliency map at different scale, $k = \{16, 32, 64\}$, convolved with a Gaussian filter of standard deviation $\sigma = 0.02 \times w$ was taken to obtain the master saliency map, this is to improve the salient region detection. The other parameters were fixed at $r = 3$, and $m = 1/10$, of the surrounding region defined by r . Table 4.1 summarize the parameters used and their respective values and symbols.

Table 4.1: Table of Parameters

Parameters	Symbols	Values
Size of blocks	k	[16,32,64]
Weights of saliency maps	w_1 w_2 w_3 and w_4	[0.1,1,0.1,1]
Number of similar regions	m	1/10 [surrounding region]
Radius	r	3
Dimension	d	7
Standard deviations	σ	0.02×512

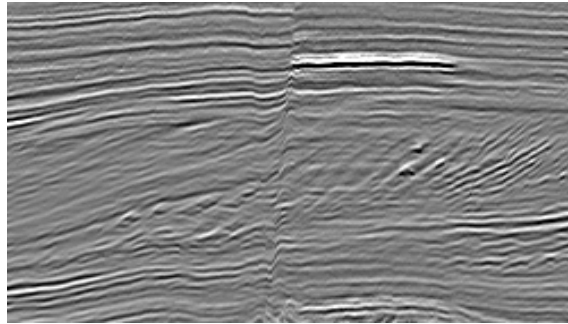


Figure 4.3: Seismic section, inline 256.

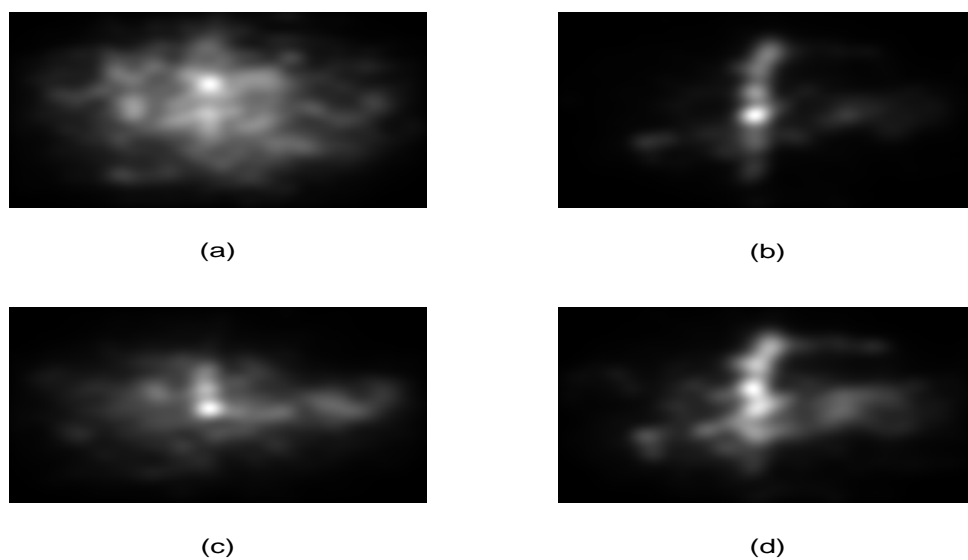


Figure 4.4: The saliency map of the attributes of inline 256 (a) Coherence (b) Curvature (c) Dip (d) Gradient.

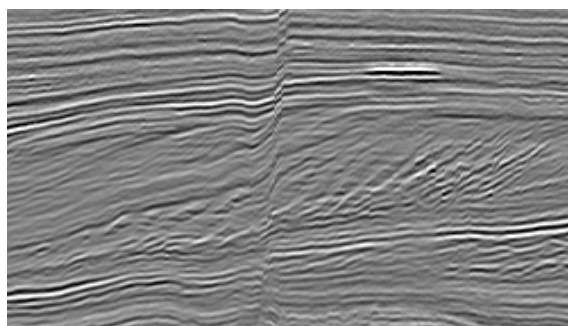


Figure 4.5: Seismic section, inline 256.

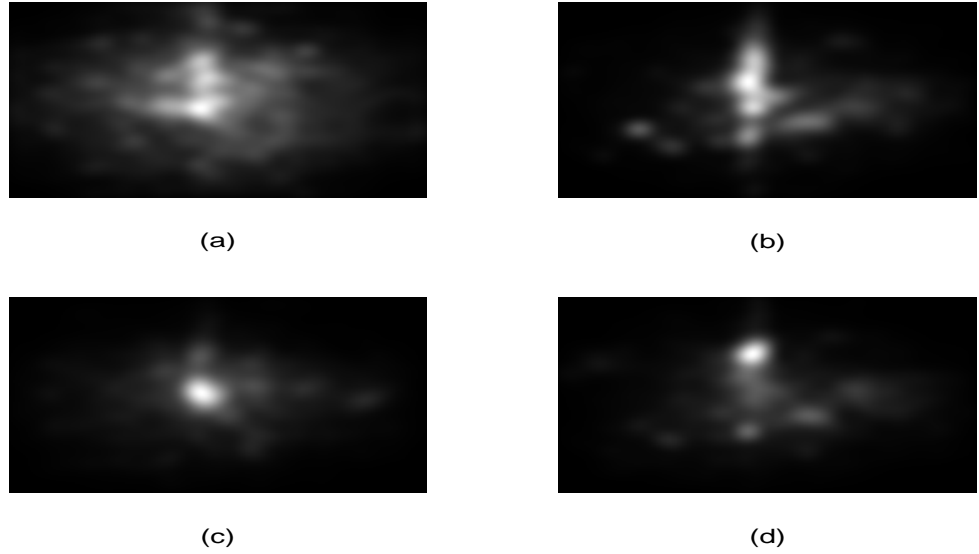


Figure 4.6: The saliency map of the attributes of inline 272 (a) Coherence (b) Curvature (c) Dip (d) Gradient.

The original seismic section inline 256 is shown in Figure 4.3 and Figure 4.4 (a)-(d) shows the saliency maps from the four different attributes which are: coherence, curvature, dip, and gradient, for inline 256, respectively. It can be observed that the fault region is highlighted in each case, the coherence saliency map is widespread but stronger at the region which corresponds to the fault region, the curvature saliency map is narrow and less spread, it highlights mainly the fault region. The dips saliency map behaves similarly to the coherency saliency map, it is spread but stronger in the region that corresponds to the fault. Finally, the gradient saliency map looks more like the curvature except that it spreads more. The narrower the saliency map the more concentrated it is in the fault region. Figure 4.5 shows the original inline 272 and Figure 4.6 (a)-(d) show the saliency

maps for inline 272. We observe that the maps behave similarly to those in Figure 4.4(a)-(d).

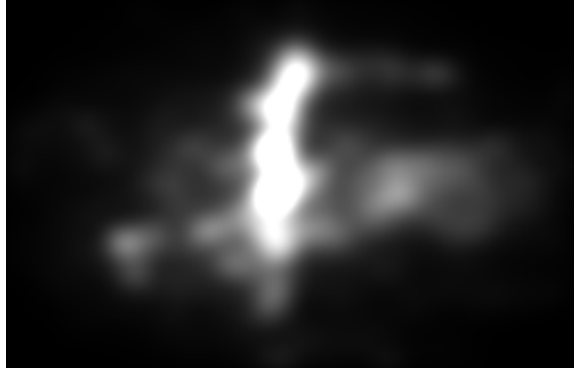


Figure 4.7: Combined saliency map of inline 256.



Figure 4.8: Combined saliency map of inline 272.

Figure 4.7 shows the saliency map obtained from the combination of the individual saliency for inline 256. We observed that the saliency map becomes more

focused after the combination and the fault region becomes more prominent. Figure 4.8 shows that the saliency map of the combined map for inline 272. Similarly it can be observe that the fault region is well highlighted and there is a shift to the left relative to that of inline 256 due to shift in fault position from inline 256 to 272.

To demonstrate how the saliency map highlights the fault region, the saliency map was overlaid on the original seismic inlines. Figure 4.9 (a) shows the original seismic inline 256 while (b) shows the overlaid saliency map. It can be observed that the brightest region of the saliency map corresponds to the fault region. Similarly, Figure 4.10 (a) shows the original inline 272 and (b) shows the overlaid saliency map on inline 272.

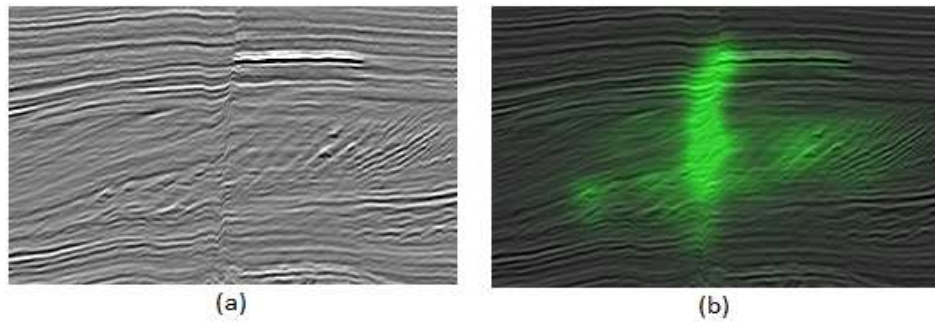


Figure 4.9: (a) inline 256 (b) overlaid saliency map.

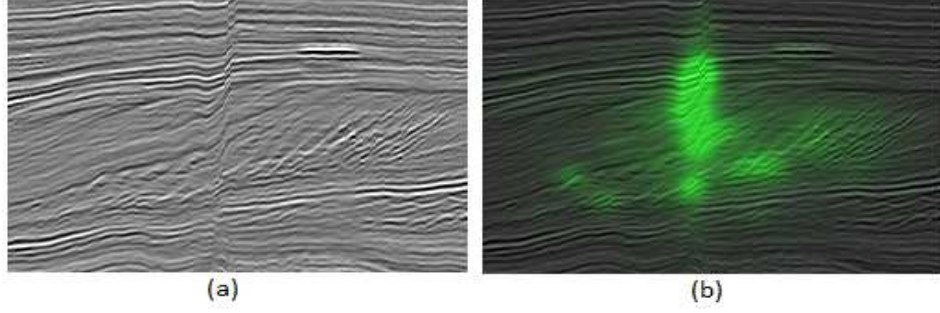


Figure 4.10: (a) inline 272 (b) overlaid saliency map.

To demonstrate the performance of the proposed method with multiple faults, the algorithm was applied on inline 249 shown in Figure 4.11 which is a section with multiple faults at different spatial scales. A similar process was followed as for inline 256 and 272. First, we computed the saliency map of different attributes. Figure 4.12(a)-(d) shows the saliency maps of coherence, curvature, dips and gradient for inline 249 respectively. We observe that curvature and gradient attributes highlights the boundary along which the faults are located while the coherence and dip spreads around with no visible information.

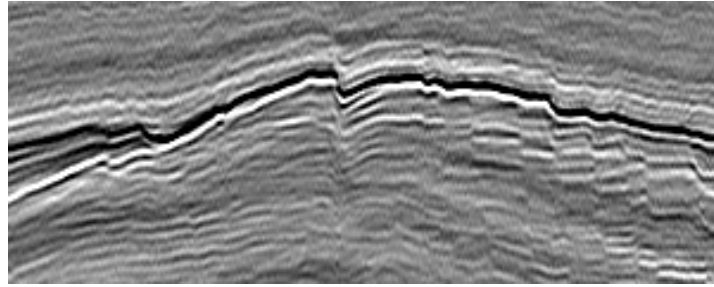


Figure 4.11: Seismic section, inline 249.

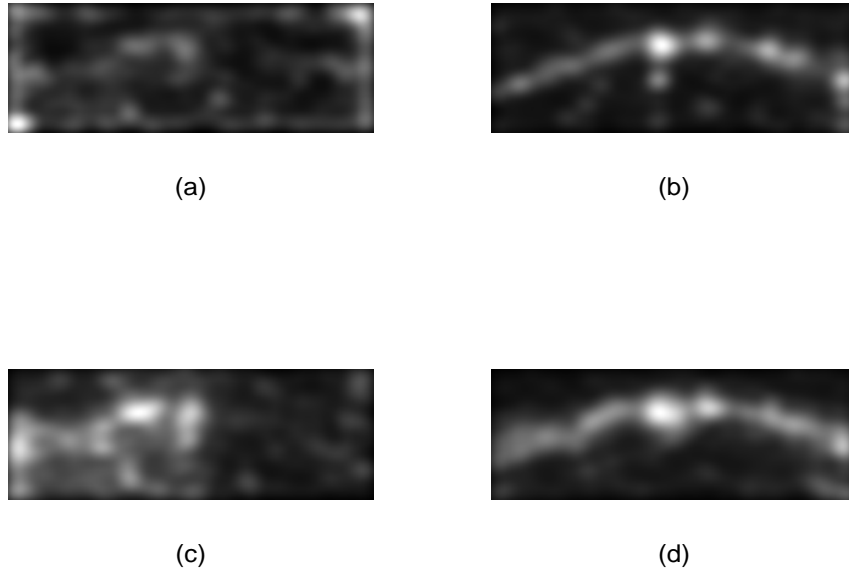


Figure 4.12: Saliency map of the attributes for inline 249 (a) Coherence (b) Curvature (c) Dip (d) Gradient.

Upon combining the different saliency maps, it can be observed, in Figure 4.13, that the individual faults points become highlighted better than the individual maps.

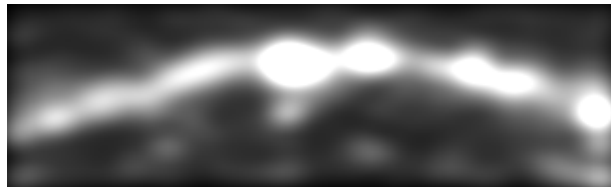


Figure 4.13: Combined saliency map for inline 249.

Figure 4.14 (a) and (b) shows the original inline 249 section and the overlaid saliency map. We observe that the fault regions are highlighted at different points which shows the ability of the algorithm to highlight multiple faults in a seismic section. Figure 4.15 to Figure 4.23 show the results for different inlines and their respective saliency maps. The saliency map in each case clearly highlights the fault regions and makes the detection of faults location easier.

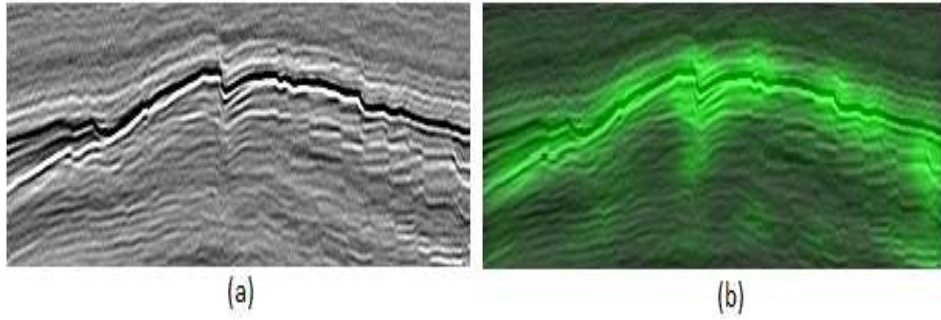


Figure 4.14: (a) Inline 249 (b) overlaid saliency map.

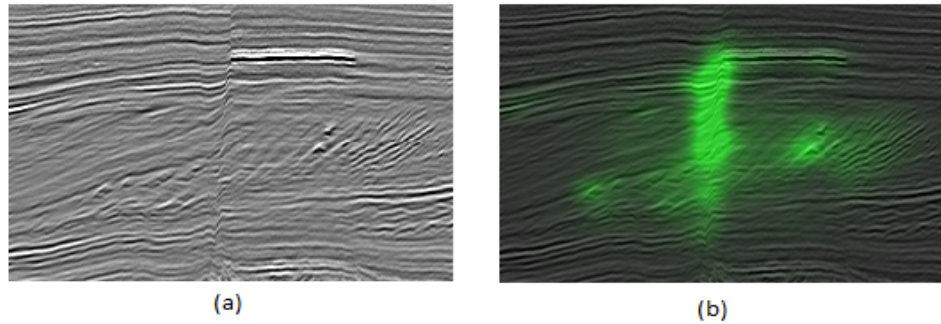


Figure 4.15: (a) inline 258 (b) overlaid saliency map.

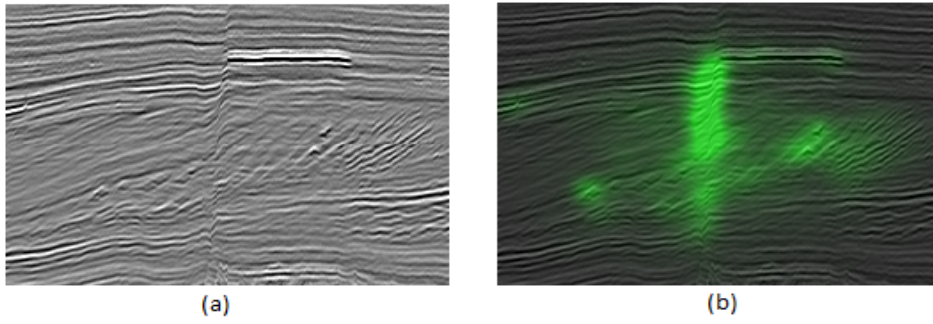


Figure 4.16: (a) inline 260 (b) overlaid saliency map.

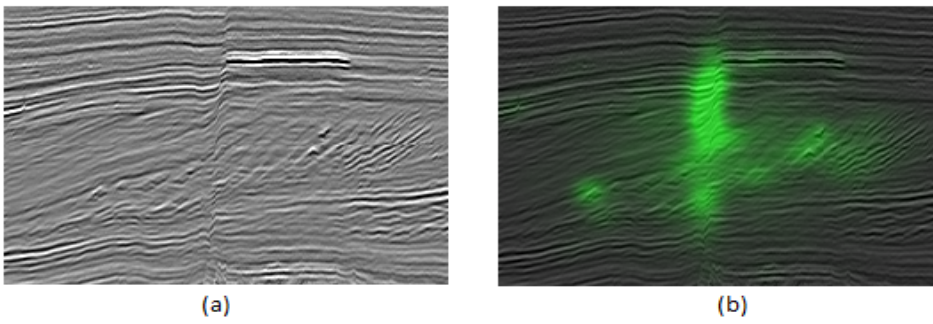


Figure 4.17: (a) inline 262 (b) overlaid saliency map.

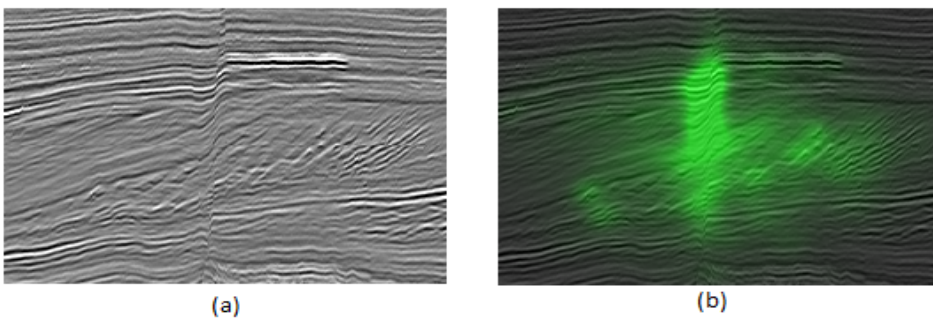


Figure 4.18: (a) inline 264 (b) overlaid saliency map.

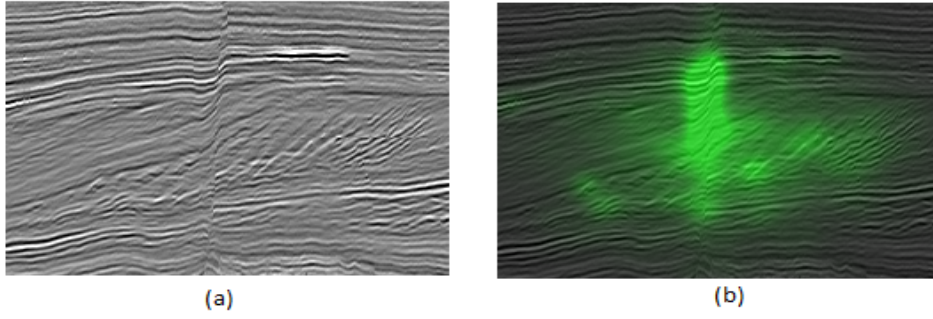


Figure 4.19: (a) inline 266 (b) overlaid saliency map.

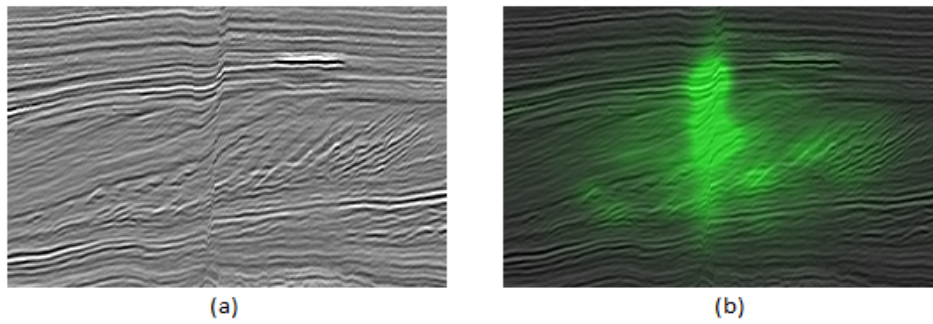


Figure 4.20: (a) inline 268 (b) overlaid saliency map.

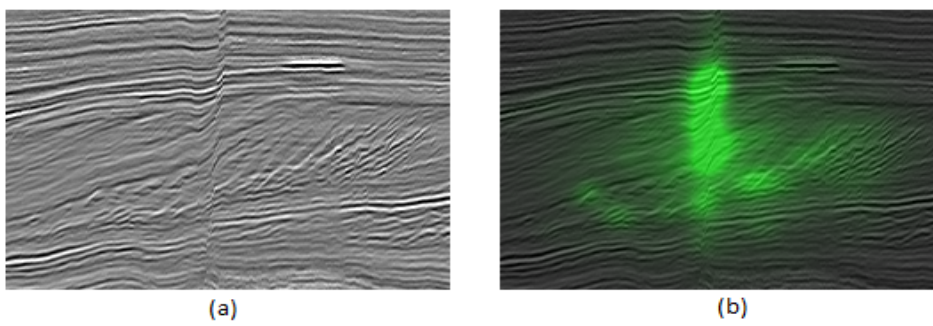


Figure 4.21: (a) inline 270 (b) overlaid saliency map.

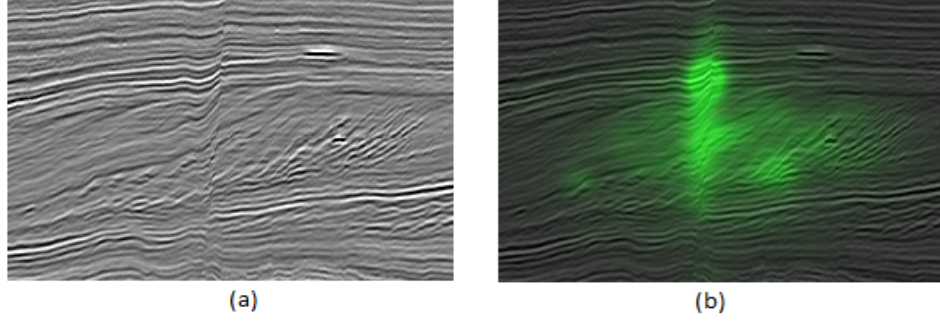


Figure 4.22: (a) inline 280 (b) overlaid saliency map.

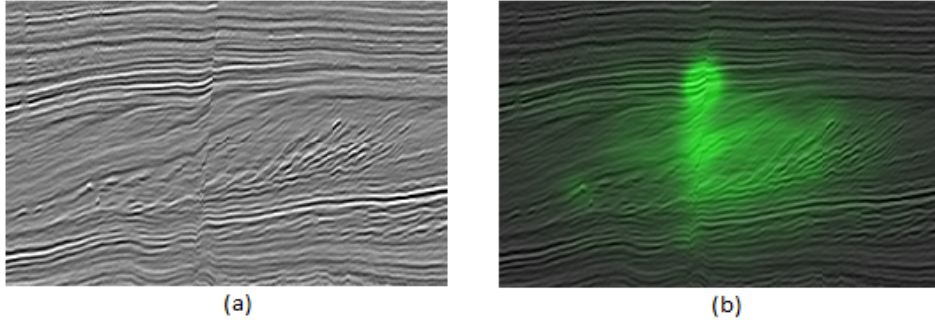


Figure 4.23: (a) inline 290 (b) overlaid saliency map.

4.8 Conclusion

The developed saliency model highlights fault regions in different seismic sections. The four attributes image gave different saliency maps. While the coherence and dips were wide spread, the gradient and curvature maps were concentrated toward the fault region. The combination of these maps gave a more consolidated saliency map that focuses mainly on the fault region. The weighting were used to reduce the effects of region that are not salient in the final map. We showed the power proposed algorithm across different types of inlines. We also demonstrated the

model ability in highlighting multiple faults.

CHAPTER 5

DELINEATING FAULT LINES

In this Chapter, we delineate and extract fault lines in 2D seismic sections over multiple stages. Delineating fault means extracting and labelling the precise fault locations in the seismic section, this gives the interpreter the precise fault location. We first obtain the variance-based coherence and most-negative curvature attributes to enhance the fault region. Then, we will apply thresholding and consider geological constraints to remove false features. We propose a method to obtain the optimal fault points through numerical optimization, and then we fit a line to label the faults accurately. The performance of the proposed technique for fault labelling is assessed objectively and compared with the ground truth. Note that fault delineation or labelling stage solely depends on the selected seismic attributes to further assist interpreters in precisely tracing fault lines

5.1 Fault Enhancement

Faults are highlighted or predicted by enhancing the discontinuities in seismic data along the reflection layers. There are several fault-sensitive seismic attributes, as discussed in Chapter 3; however, in our study we focus on the variance-based coherence and curvature attributes. Specifically, we consider the variance-based coherence, introduced in subsection 3.1.2, to have an initial estimate of the possible fault points through a proper thresholding. Then, we further refine the results by considering most-negative curvature attribute to determine the optimal fault points numerically.

Both variance-based coherence and most-negative curvature are computed for a specific seismic section. Prominent faults are generally highlighted by the variance-based coherence, while curvature attributes discern the details of mild or subtle faults. An example of variance-based coherence attribute for inline 256 and inline 272 is shown in Figure 5.1 (a) and (b), respectively.

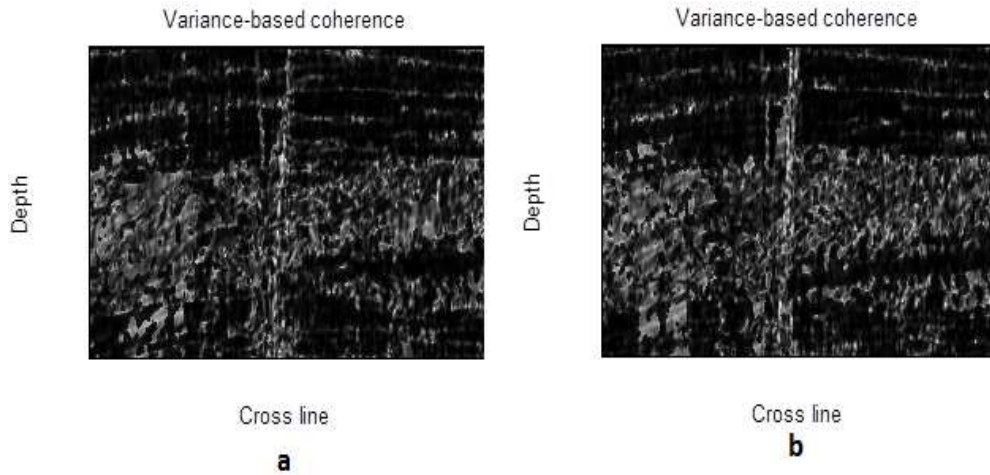


Figure 5.1: Variance-based coherence of (a) inline 256 (b) inline 272.

The white regions indicate low coherence between seismic traces in Figure 5.1 and a possibility of fault; however, dark regions represent higher coherence and less chance of faults. Figure 5.2 (a) and (b) depicts the most-negative curvature of inline 256 and 272, respectively.

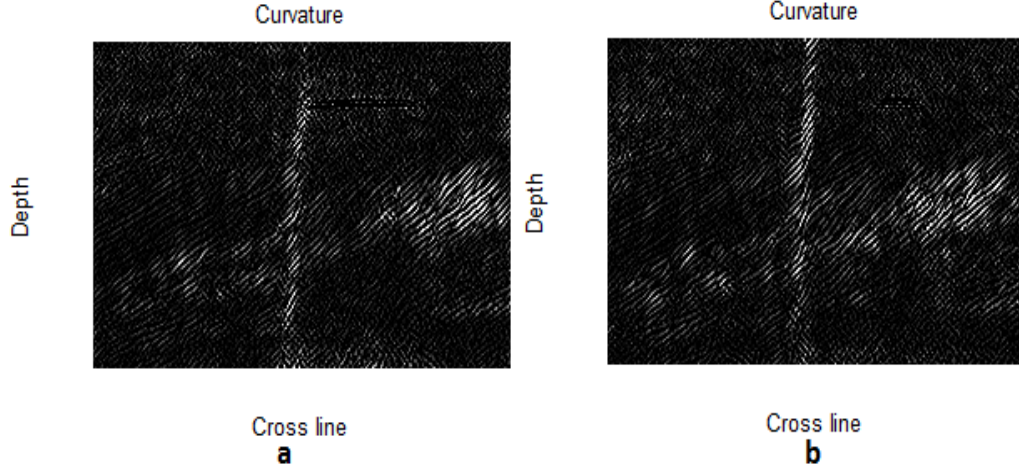


Figure 5.2: Most-negative curvature of (a) inline 256 (b) inline 272.

Here, the curvature attribute is effective in specifying the fault geometry, where anomalous values are introduced over the fault with high positive curvature on upthrown side and high negative curvature on downthrown side. Note that in Figure 5.2 both inlines have similar fault geometries.

5.2 Global Thresholding

In this section, we highlight the likely fault points by applying a global threshold on the variance-based coherence for a seismic section. A high value of the variance-based coherence, $c_v(x, y)$, indicates a higher probability that the point lies in a fault region, while a lower value indicates that the point is likely to be a non-fault

point.

A threshold is determined empirically and applied to the variance-based coherence using a 15×15 window. If the mean of window is less than a predefined value, then it is masked; otherwise, a threshold of 0.7 is applied. The interpreter can determine this threshold empirically. We select in our case a mean of 2.5 for the considered window. The binary image is obtained by

$$b(x, y) = \begin{cases} 1, & \text{if } c_v(x, y) \geq 0.7 \\ 0, & \text{otherwise} \end{cases}, \quad (5.1)$$

where x and y are the cross line and depth directions, respectively.

In Figure 5.3 (a), we present the binary image for inline 256 after thresholding variance-based coherence. The white pixels highlight the likely fault points, which are scattered over a wide region.

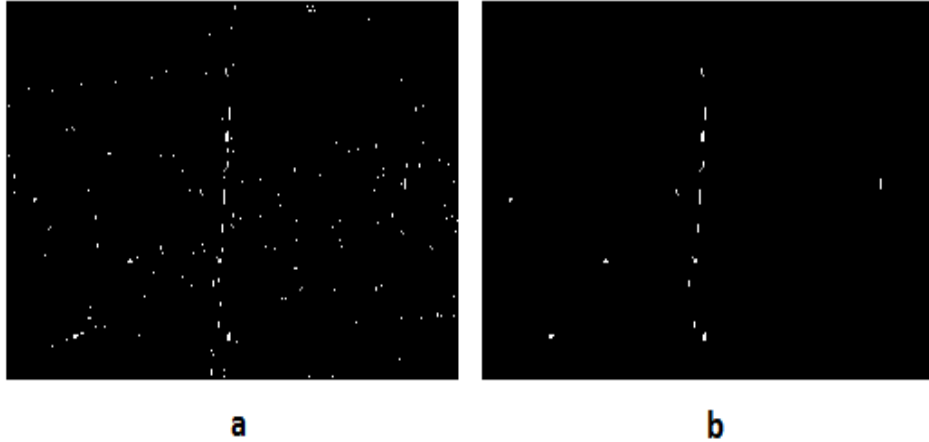


Figure 5.3: Binary image for inline 256 after (a) thresholding $c_v(x, y)$ (b) false feature removal.

Similarly, we observe in Figure 5.4 (a) the likely fault points for inline 272 after we apply the threshold to $c_v(x, y)$. We notice that the false fault points are inevitable after thresholding. Therefore, we adopt the double thresholding technique in [1] to remove such false features.



Figure 5.4: Binary image for inline 272 after (a) thresholding $c_v(x, y)$ (b) false feature removal.

We define absolute and lateral distances, which represent the spatial distance and projection distance between two lines, respectively. The absolute distance (AD) is given by

$$AD = \|\mathbf{G}_i - \mathbf{G}_{i-1}\|_2^2, \quad (5.2)$$

where \mathbf{G}_i , $i = 1, 2, \dots, n$ are lines with start position $(x_{s,i}, y_{s,i})$ and the end position

$(x_{e,i}, y_{e,i})$. The length of \mathbf{G}_i is

$$L(\mathbf{G}_i) = \sqrt{(x_{s,i} - x_{e,i})^2 + (y_{s,i} - y_{e,i})^2}. \quad (5.3)$$

These lines are ordered according to their vertical spatial positions [1]. To obtain the lateral distance (LD), we denote the mid-point vector of line \mathbf{G}_i as

$$\mathbf{m}_i = \left(\frac{x_{s,i} + x_{e,i}}{2}, \frac{y_{s,i} + y_{e,i}}{2} \right). \quad (5.4)$$

The lateral distance is defined as the projection of the vector connecting \mathbf{m}_i and \mathbf{m}_{i-1} on the direction perpendicular to \mathbf{G}_{i-1} , which is given by

$$LD = |(\mathbf{m}_i - \mathbf{m}_{i-1}) \cdot \mathbf{v}_{i-1,\perp}|, \quad (5.5)$$

where $\mathbf{v}_{i-1,\perp}$ is the unit vector orthogonal to \mathbf{G}_{i-1} .

We have applied the double threshold to the considered seismic sections to remove the false fault points. In Figure 5.3 (b) above, we show the binary image after removing the false features for inline 256. Similarly, the false fault points are removed by the same technique for inline 272 as shown in Figure 5.4 (b). We observe that most of those false features have been eliminated successfully.

After removing the false features, we connect all the highlighted points to label the fault in the seismic section. The connected points for inline 256 and inline 272 are shown in Figure 5.5 (a) and (b), respectively.



Figure 5.5: Connected points after false feature removal for (a) inline 256 (b) inline 272.

Clearly, these lines in Figure 5.5 are not accurate to represent the fault line in the seismic sections. Hence, there is a need to enhance the fault labeling and find the optimal fault points by considering the curvature attribute through numerical optimization, which is discussed in the next section.

5.3 Numerical Optimization

In this section, we combine the information from the variance-based coherence and most-negative curvature attributes to label the faults in seismic sections in an optimal way.

Let $P_c = (x_c(i), y_c(i)), i = 1, 2, \dots$ be a point obtained from the line in Figure 5.5 where $x_c(i)$ and $y_c(i)$ are the coordinates of the cross line and depth directions, respectively, at point i . This coordinate is used with a particular radius r_s to search in a group of points in the variance-based coherence along the cross line that corresponds to the local maximum variance value. We also use the same

coordinates to search for a group of points that correspond to the local maximum of the most-negative curvature. We obtain two sets of coordinates from the variance and curvature attributes. Then, we combine the set of coordinates to form a single coordinates by taking their averages.

Let $x_m(i)$ be the local maxima obtained from the search along the cross line direction in the variance-based coherence, which is given by

$$x_m(i) = \arg \max_{x \in [-r_s + x_c(i), x_c(i) + r_s]} c_v(x, y_c(i)), \quad (5.6)$$

and the local maxima obtained from the search along the most-negative curvature, $x_n(i)$, is given by

$$x_n(i) = \arg \max_{x \in [-r_s + x_c(i), x_c(i) + r_s]} K_{neg}(x, y_c(i)). \quad (5.7)$$

The average of these two points is

$$x_w(i) = \frac{x_m(i) + x_n(i)}{2}. \quad (5.8)$$

Now, each cross line has two points that are candidate to be a fault point, one point is $x_c(i)$, which is obtained from the original line and the second point is $x_w(i)$, which is obtained from (5.8). Then, we decide on the location in the interval $[x_w(i), x_c(i)]$.

We determine the optimal location of the fault point based on the objective

function as in [1]

$$\hat{x} = \arg \max_x \lambda_1 \|x - x_c\|_2^2 + \lambda_2 \|x - x_w\|_2^2, \quad (5.9)$$

where λ_1 and λ_2 represent the weight of $x_c(i)$ and $x_w(i)$ respectively, and \hat{x} is the optimal point that we will use for fault labeling. For the considered seismic sections, $\lambda_1 = 0.2$ and $\lambda_2 = 0.8$.

We demonstrate the performance of our proposed optimization using coherence and curvature attributes. We illustrate the optimization using the variance-based coherence for inline 256 and 272 respectively in Figure 5.6 (a) and (b). In Figure 5.7 (a) and (b), we show the optimization using the curvature attribute for inline 256 and 272, respectively. Then, we show the optimization using the combined attributes, i.e. variance-based and curvature attributes, in Figure 5.8 (a) and (b).

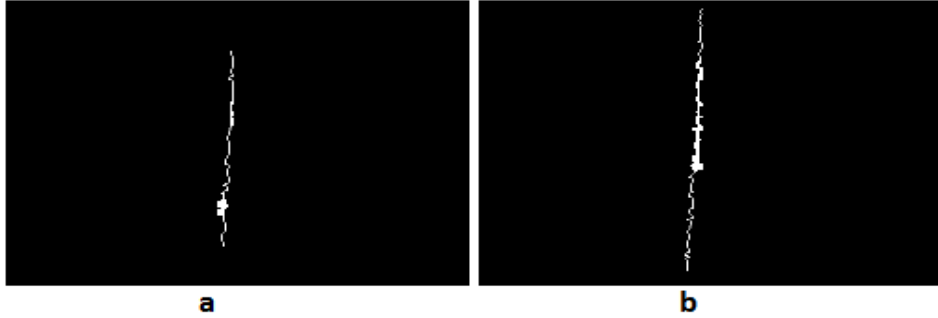


Figure 5.6: Optimization using variance-based coherence for (a) inline 256 (b) inline 272.



Figure 5.7: Optimization using curvature for (a) inline 256 (b) inline 272.

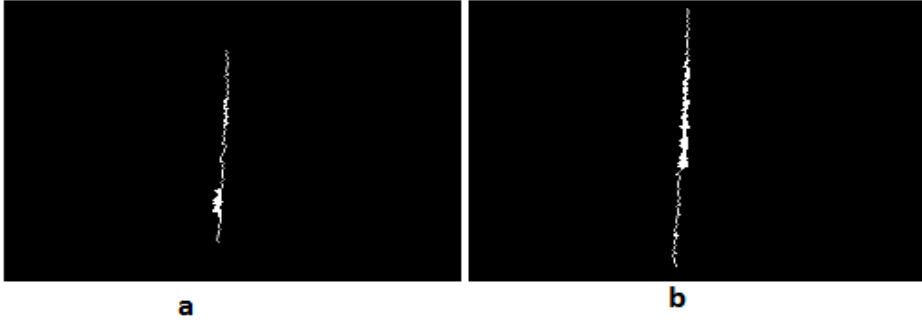


Figure 5.8: Optimization using both variance-based coherence and curvature attributes for (a) inline 256 (b) inline 272.

We observe that the line in Figure 5.6 (a) and (b) has rough edges while the one in Figure 5.7 (a) and (b) has zigzag shape. In Figure 5.8, the line is a balance between roughness and zigzag shape, and gives better details about the fault line.

5.4 Labeling Faults

In this section, we label the faults and avoid the zigzag shape of the optimized points in Figure 5.8 by fitting a line to accurately delineate faults in seismic sections. Figure 5.9 (a) and (b) shows the labeled inline 256 and inline 272,

respectively. We observe that the labeled faults based on the proposed approach are similar in the two seismic sections.

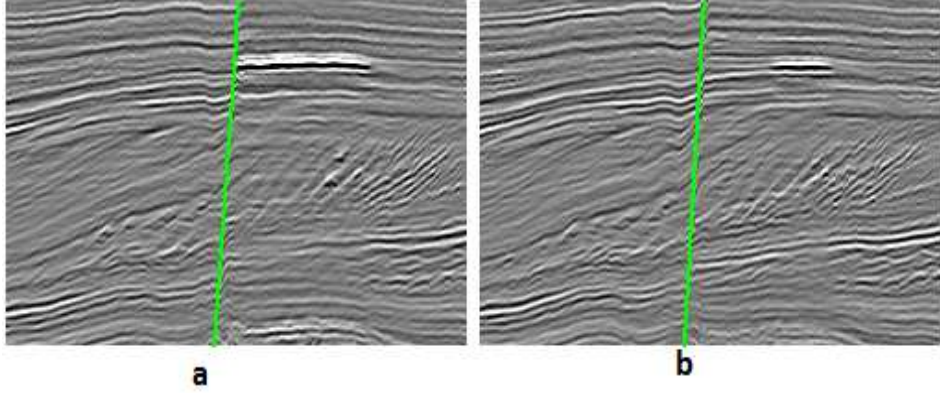


Figure 5.9: Labeled faults for (a) inline 256 (b) inline 272.

We compare our approach with the ground truth, which is a manually labeled fault, and apply it to the inlines 256 and 272. Figure 5.10 (a) and (b) shows the labeled fault based on the proposed approach (in green) and the ground truth (in red) comparison for inline 256 and inline 272, respectively.

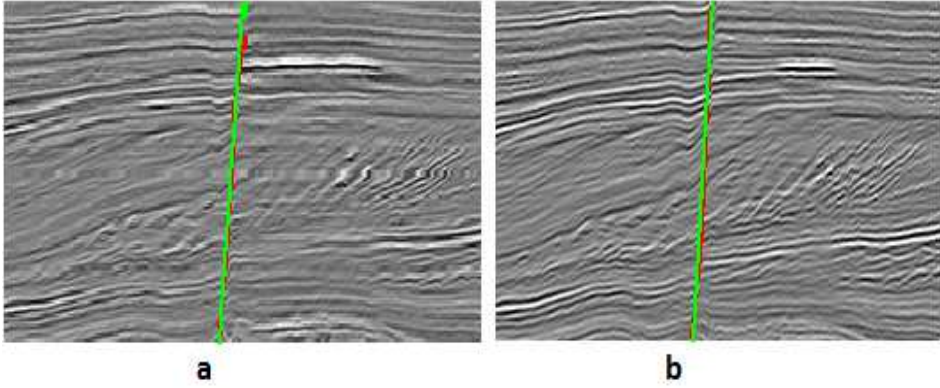


Figure 5.10: Proposed labeled faults (green) compared with ground truth (red) for (a) inline 256 (b) inline 272.

We observe from Figure 5.10 that the proposed approach yields fault labels

that are very close to the ground truth.

This algorithm has also been applied to inline 249 with multiple fault. Figure 5.11 shows the labeling for multiple faults. We notice that several fault points are extracted, and the fault lines are generated.

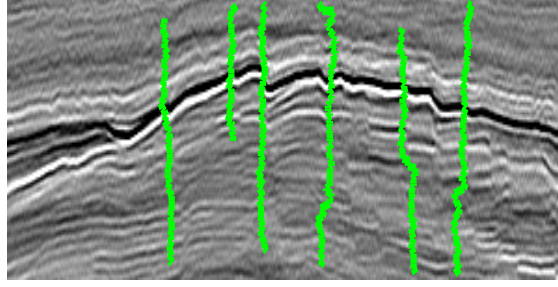


Figure 5.11: The labelled faults of inline 249 with multiple fault.

5.5 Similarity Index Measurement

There is a need to objectively evaluate the similarity between the ground truth and the proposed algorithm. In this section, we apply Fréchet distance-based similarity index (SalSIM), which is originally proposed for salt domes by Wang et al. [80].

We use a local analysis window that identifies a pair of segments. This analysis window is moved along the ground truth and the Fréchet distance of the pair of the local segments is computed. For a total number of segments N_d , a sequence of distances $\mathbf{d} = [d_i], i = 1, 2, \dots, N_d$ is obtained. The mean and standard deviation of \mathbf{d} are computed and denoted as μ_d and σ_d . These are considered as the local parameters. A global Fréchet distance, d_{max} , of the entire boundary is also

calculated and used as the global parameter. The SalSIM index is given as

$$SalSIM = e^{-\alpha(\mu_d + \sigma_d)} e^{-\beta d_{max}}, \quad (5.10)$$

where α and β are the empirically determined normalization factor. The SalSIM index varies from 0 to 1, indicating the minimum and maximum similarity between the labeled fault and the ground truth.

Figure 5.12 compares SalSIM indices of the proposed method and the method used in [1].

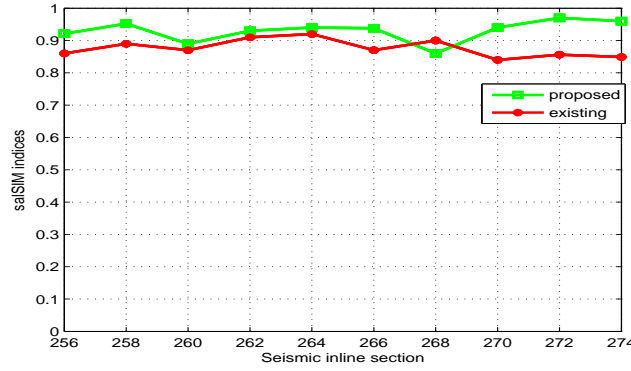


Figure 5.12: SalSIM indices of the proposed method (green) with the Hough transform based method in [1] (red).

We observe that the proposed algorithm outperforms the Hough transform based one in [1]. This due to the combined information of variance-based coherence and curvature attributes in the optimization stage and the curve fitting. Our approach also have a better computational complexity as it takes only 1.2s to run compared to the Hough transforms which takes about 5.3s to run in Matlab.

Figure 5.13 to Figure 5.19 show the comparison of the proposed approach and the manually labelled fault region, we observe from the figures that proposed approach (green) labels fault very close to the ground truth (red) this confirms the SalSM index being close to 1.

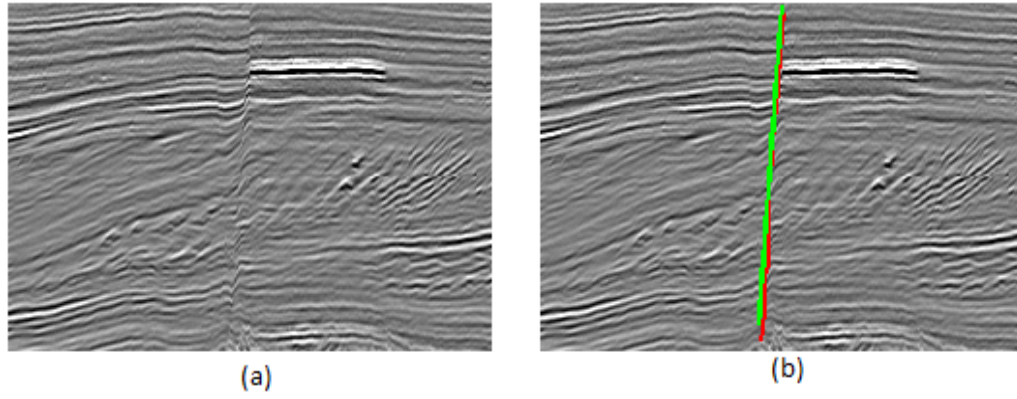


Figure 5.13: (a) inline 258 (b) Proposed labelled faults (green) compared with ground truth (red) for inline 258

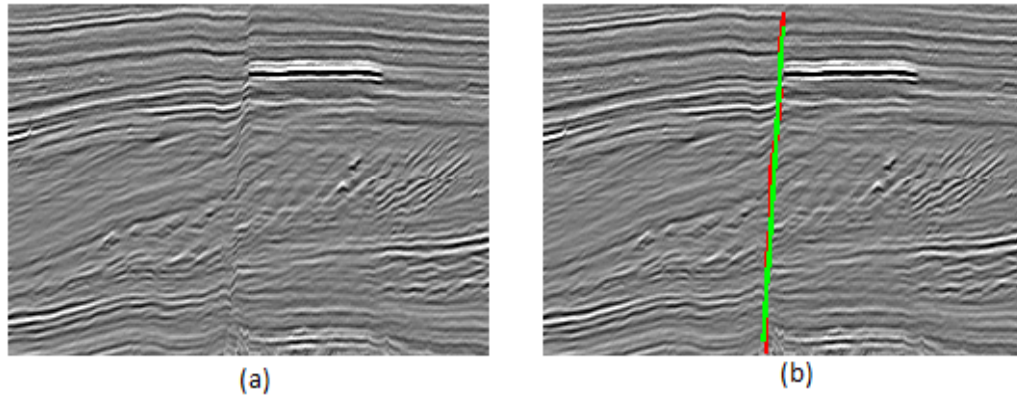


Figure 5.14: (a) inline 260 (b) Proposed labelled faults (green) compared with ground truth (red) for inline 260

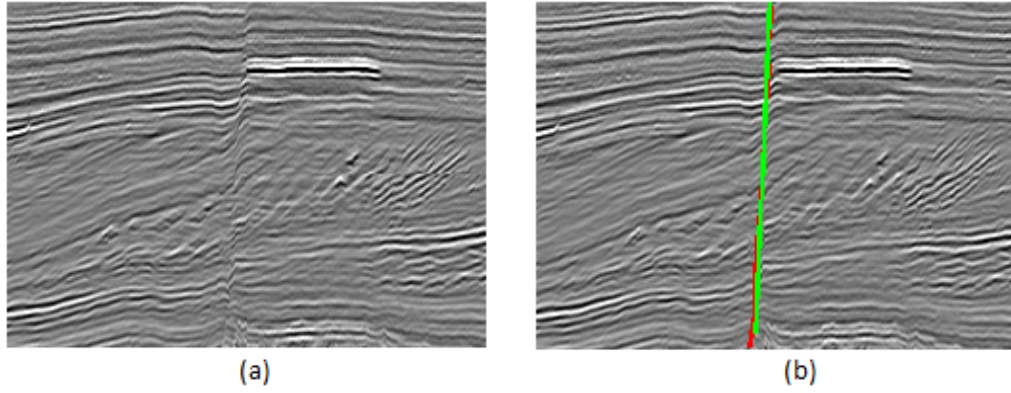


Figure 5.15: (a) inline 262 (b) Proposed labelled faults (green) compared with ground truth (red) for inline 262

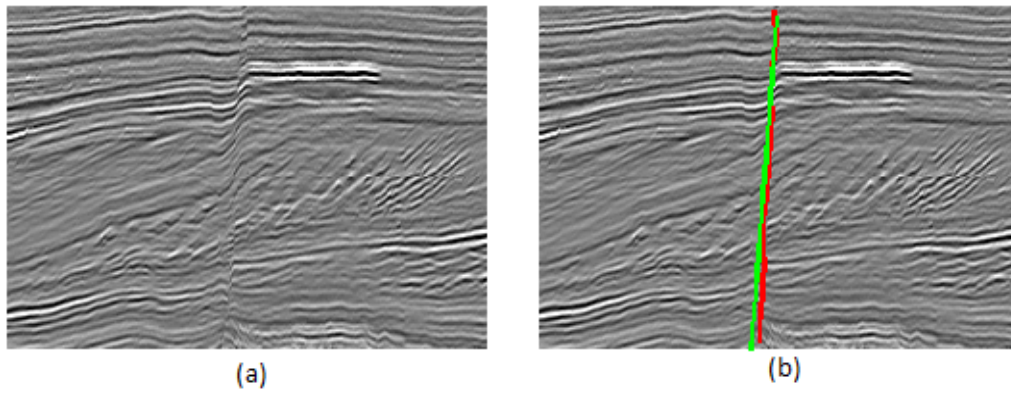


Figure 5.16: (a) inline 264 (b) Proposed labelled faults (green) compared with ground truth (red) for inline 264

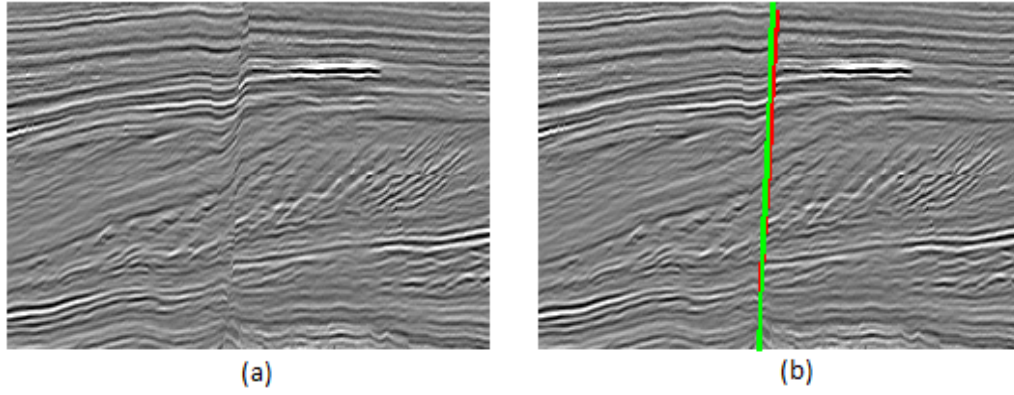


Figure 5.17: (a) inline 266 (b) Proposed labelled faults (green) compared with ground truth (red) for inline 266

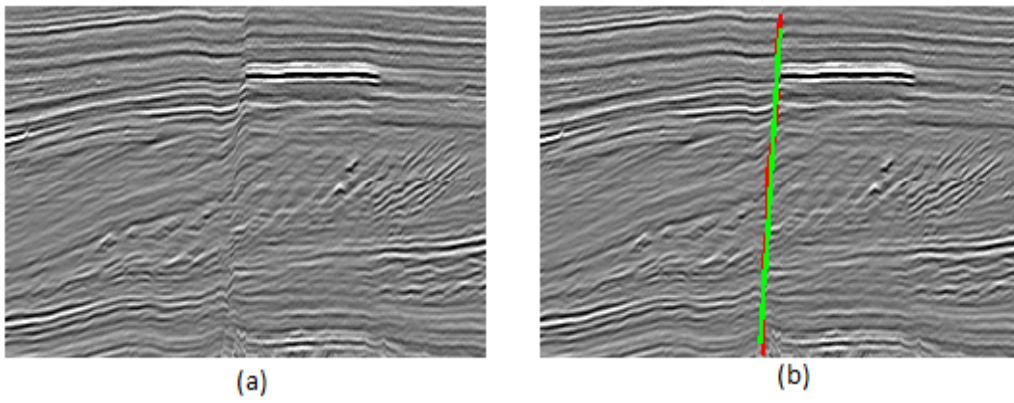


Figure 5.18: (a) inline 268 (b) Proposed labelled faults (green) compared with ground truth (red) for inline 268

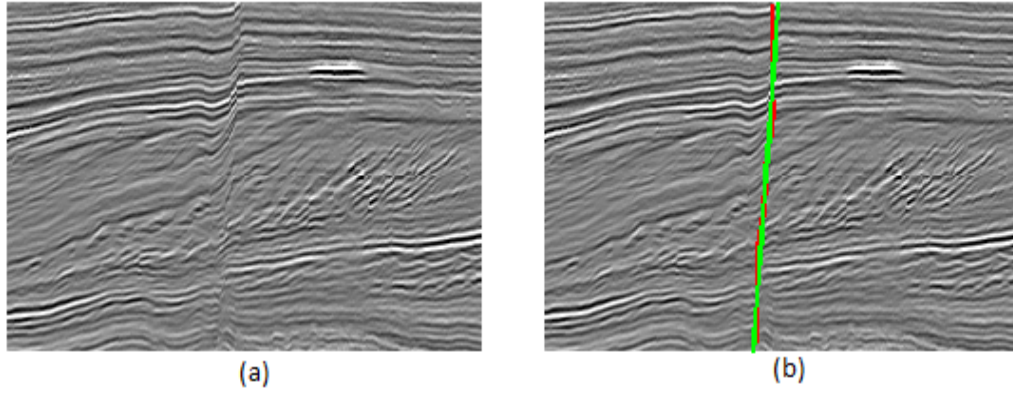


Figure 5.19: (a) inline 274 (b) Proposed labelled faults (green) compared with ground truth (red) for inline 274

CHAPTER 6

CONCLUSION AND FUTURE WORK

6.1 Conclusion

In our work, we introduced the concept of saliency to highlight faults in seismic sections. The algorithm was tested on a series of inlines extracted from a 3D seismic volume from Netherland offshore F3 block North sea [7]. The results show a high potential of using the saliency map for fault visualization and location. The fault labelling was robust and track fault within a fraction of time normally spent by seismic interpreters. The work is not only limited to a single fault, but capable of detecting multiple faults in the seismic data set. The work developed here has a strong relevance to the oil industry for quick fault checking and would ease the tasks of the interpreters so that time is given to other task. The success in using the saliency map is highly dependent upon the careful selection of seismic

attributes that are sensitive to faults such as coherency , curvature , dips, and gradient attributes. The combination of the individual saliency maps provided a more robust tool for highlighting fault regions. The fault labelling also plays a very important role as it automatically locates and labels the fault points in the seismic data. Since interpreters deal with a very large amount of data set, fault labelling will speed up the process of interpretation and will provide a reliable and efficient way of labelling fault positions. The proposed algorithm has lower computational cost and produces accurate results compared to existing approaches.

6.2 Future work

In the future, we propose a number of new directions; the saliency could be extended for 3D seismic data , the saliency also has a shortcoming of not giving the exact length of the fault, more investigation could be performed in this domain. The saliency can also be extended to 3D such that it can be applied to a 3D seismic data volumes directly. The Fault labelling can also be extended to 3D data sets. More investigation can be performed on the combination of attributes that produces an optimal and robust saliency map.

REFERENCES

- [1] Z. Wang and G. AlRegib, “Fault detection in seismic datasets using hough transform,” in *2014 International Conference on Acoustics, Speech and Signal Processing (ICASSP)*. IEEE, 2014, pp. 2372–2376.
- [2] A. Aydin, “Fractures, faults, and hydrocarbon entrapment, migration and flow,” *Marine and petroleum geology*, vol. 17, no. 7, pp. 797–814, 2000.
- [3] K. M. Tingdahl and M. De Rooij, “Semi-automatic detection of faults in 3d seismic data,” *Geophysical Prospecting*, vol. 53, no. 4, pp. 533–542, 2005.
- [4] W. A. Mousa and A. A. Al-Shuhail, “Processing of seismic reflection data using matlab,” *Synthesis Lectures on Signal Processing*, vol. 5, no. 1, pp. 1–97, 2011.
- [5] D. W. Vasco, A. Datta-Gupta, R. Behrens, P. Condon, and J. Rickett, “Seismic imaging of reservoir flow properties: Time-lapse amplitude changes,” *Geophysics*, vol. 69, no. 6, pp. 1425–1442, 2004.
- [6] B. Biondi, S. Fomel, and N. Chemingui, “Azimuth moveout for 3-d prestack imaging,” *Geophysics*, vol. 63, no. 2, pp. 574–588, 1998.

- [7] “OpendTect kernel description,” <https://opendtect.org/osr/>,.
- [8] H. M. Basir, A. Javaherian, and M. T. Yarakı, “Multi-attribute ant-tracking and neural network for fault detection: a case study of an iranian oilfield,” *Journal of Geophysics and Engineering*, vol. 10, no. 1, p. 015009, 2013.
- [9] Z. Yan, H. Gu, and C. Cai, “Automatic fault tracking based on ant colony algorithms,” *Computers & Geosciences*, vol. 51, pp. 269–281, 2013.
- [10] C. Zhang, C. Frogner, M. Araya-Polo, and D. Hohl, “Machine-learning based automated fault detection in seismic traces,” in *76th EAGE Conference and Exhibition*, 2014.
- [11] N. M. AlBinHassan and K. M. Marfurt, “Fault detection using hough transforms,” in *73rd Annual International Meeting, SEG, Expanded Abstracts*. Society of Exploration Geophysicists, 2003, pp. 1719–721.
- [12] P. Jacquemin and J.-L. Mallet, “Automatic faults extraction using double hough transform,” in *2005 SEG Annual Meeting*. Society of Exploration Geophysicists, 2005.
- [13] Z. Wang, G. AlRegib *et al.*, “Automatic fault surface detection by using 3d hough transform,” in *2014 SEG Annual Meeting*. Society of Exploration Geophysicists, 2014.
- [14] Z. Wang, Z. Long, G. AlRegib, A. Asjad, and M. A. Deriche, “Automatic fault tracking across seismic volumes via tracking vectors,” in *2014 International Conference on Image Processing (ICIP)*. IEEE, 2014, pp. 5851–5855.

- [15] D. Hale, “Structure-oriented smoothing and semblance,” *CWP report*, vol. 635, pp. 261–270, 2009.
- [16] M. Bahorich and S. Farmer, “3-d seismic discontinuity for faults and stratigraphic features: The coherence cube,” *The leading edge*, vol. 14, no. 10, pp. 1053–1058, 1995.
- [17] K. J. Marfurt, R. L. Kirlin, S. L. Farmer, and M. S. Bahorich, “3-d seismic attributes using a semblance-based coherency algorithm,” *Geophysics*, vol. 63, no. 4, pp. 1150–1165, 1998.
- [18] A. Gersztenkorn and K. J. Marfurt, “Eigenstructure-based coherence computations as an aid to 3-d structural and stratigraphic mapping,” *Geophysics*, vol. 64, no. 5, pp. 1468–1479, 1999.
- [19] A. E. Barnes, “Theory of 2-d complex seismic trace analysis,” *Geophysics*, vol. 61, no. 1, pp. 264–272, 1996.
- [20] A. E. Barnes, “Weighted average seismic attributes,” *Geophysics*, vol. 65, no. 1, pp. 275–285, 2000.
- [21] K. J. Marfurt, “Robust estimates of 3d reflector dip and azimuth,” *Geophysics*, vol. 71, no. 4, pp. P29–P40, 2006.
- [22] A. Roberts, “Curvature attributes and their application to 3 d interpreted horizons,” *First break*, vol. 19, no. 2, pp. 85–100, 2001.

- [23] S. Al-Dossary and K. J. Marfurt, “3d volumetric multispectral estimates of reflector curvature and rotation,” *Geophysics*, vol. 71, no. 5, pp. P41–P51, 2006.
- [24] A. E. Barnes, “A filter to improve seismic discontinuity data for fault interpretation,” *Geophysics*, vol. 71, no. 3, pp. P1–P4, 2006.
- [25] G. Machado, A. Alali, B. Hutchinson, O. Olorunsola, and K. J. Marfurt, “Display and enhancement of volumetric fault images,” *Interpretation*, vol. 4, no. 1, pp. SB51–SB61, 2016.
- [26] W.-K. Jeong, R. Whitaker, and M. Dobin, “Interactive 3d seismic fault detection on the graphics hardware,” *Volume Graphics*, 2006.
- [27] F. Admasu, S. Back, and K. Toennies, “Autotracking of faults on 3d seismic data,” *Geophysics*, vol. 71, no. 6, pp. A49–A53, 2006.
- [28] Z. Wang, D. Temel, and G. AlRegib, “Fault detection using color blending and color transformations,” in *2014 Global Conference on Signal and Information Processing (GlobalSIP)*. IEEE, 2014, pp. 999–1003.
- [29] I. Cohen, N. Coult, and A. A. Vassiliou, “Detection and extraction of fault surfaces in 3d seismic data,” *Geophysics*, vol. 71, no. 4, pp. P21–P27, 2006.
- [30] B. Zhang, Y. Liu, M. Pelissier, and N. Hemstra, “Semiautomated fault interpretation based on seismic attributes,” *Interpretation*, vol. 2, no. 1, pp. SA11–SA19, 2014.

- [31] F. Admasu and K. Toennies, “Automatic method for correlating horizons across faults in 3d seismic data,” in *2004 Conference on Computer Vision and Pattern Recognition (CVPR)*, vol. 1. IEEE, 2004, pp. I–114.
- [32] M. Machado and M. Gattass, “Fault identification using competitive learning,” in *10th International Congress of the Brazilian Geophysical Society*, 2007.
- [33] D. Gibson, M. Spann, and J. Turner, “Automatic fault detection for 3d seismic data.” in *7th Digital Image Computing: Techniques and Applications (DICTA)*. Citeseer, 2003, pp. 821–830.
- [34] L. Itti, C. Koch, and E. Niebur, “A model of saliency-based visual attention for rapid scene analysis,” *IEEE Transactions on Pattern Analysis & Machine Intelligence*, no. 11, pp. 1254–1259, 1998.
- [35] D. Gao and N. Vasconcelos, “Integrated learning of saliency, complex features, and object detectors from cluttered scenes,” in *Computer Society Conference on Computer Vision and Pattern Recognition (CVPR)*, vol. 2. IEEE, 2005, pp. 282–287.
- [36] D. Gao and N. Vasconcelos, “Discriminant saliency for visual recognition from cluttered scenes,” in *Advances in neural information processing systems*, 2004, pp. 481–488.

- [37] D. Gao, V. Mahadevan, and N. Vasconcelos, “On the plausibility of the discriminant center-surround hypothesis for visual saliency,” *Journal of vision*, vol. 8, no. 7, pp. 13–13, 2008.
- [38] X. Hou and L. Zhang, “Dynamic visual attention: Searching for coding length increments,” in *Advances in neural information processing systems*, 2009, pp. 681–688.
- [39] L. Itti and P. F. Baldi, “Bayesian surprise attracts human attention,” in *Advances in neural information processing systems*, 2005, pp. 547–554.
- [40] N. D. Bruce and J. K. Tsotsos, “A statistical basis for visual field anisotropies,” *Neurocomputing*, vol. 69, no. 10, pp. 1301–1304, 2006.
- [41] A. Oliva, A. Torralba, M. S. Castelhana, and J. M. Henderson, “Top-down control of visual attention in object detection,” in *2003 International conference on Image processing (ICIP)*, vol. 1. IEEE, 2003, pp. I–253.
- [42] U. Rutishauser, D. Walther, C. Koch, and P. Perona, “Is bottom-up attention useful for object recognition?” in *Proceedings of the 2004 IEEE Computer Society Conference on Computer Vision and Pattern Recognition (CVPR)*, vol. 2. IEEE, 2004, pp. II–37.
- [43] C. Siagian and L. Itti, “Rapid biologically-inspired scene classification using features shared with visual attention,” *IEEE Transactions on Pattern Analysis and Machine Intelligence*, vol. 29, no. 2, pp. 300–312, 2007.

- [44] L. Zhang, M. H. Tong, and G. W. Cottrell, “Sunday: Saliency using natural statistics for dynamic analysis of scenes,” in *Proceedings of the 31st Annual Cognitive Science Conference*, 2009.
- [45] Z. Wang, L. Lu, and A. C. Bovik, “Video quality assessment based on structural distortion measurement,” *Signal processing: Image communication*, vol. 19, no. 2, pp. 121–132, 2004.
- [46] R. Achanta, S. Hemami, F. Estrada, and S. Susstrunk, “Frequency-tuned salient region detection,” in *International Conference on Computer Vision and Pattern Recognition (CVPR)*. IEEE, 2009, pp. 1597–1604.
- [47] S. Avidan and A. Shamir, “Seam carving for content-aware image resizing,” in *ACM Transactions on graphics (TOG)*, vol. 26, no. 3. ACM, 2007, p. 10.
- [48] M. Cheng, N. J. Mitra, X. Huang, P. H. Torr, and S. Hu, “Global contrast based salient region detection,” *IEEE Transactions on Pattern Analysis and Machine Intelligence*, vol. 37, no. 3, pp. 569–582, 2015.
- [49] R. Achanta, F. Estrada, P. Wils, and S. Süssstrunk, “Salient region detection and segmentation,” in *Computer Vision Systems*. Springer, 2008, pp. 66–75.
- [50] Y.-F. Ma and H.-J. Zhang, “Contrast-based image attention analysis by using fuzzy growing,” in *Proceedings of the 11th ACM international conference on Multimedia*. ACM, 2003, pp. 374–381.
- [51] Y. Hu, X. Xie, W.-Y. Ma, L.-T. Chia, and D. Rajan, “Salient region detection using weighted feature maps based on the human visual attention model,” in

- Advances in Multimedia Information Processing-PCM*. Springer, 2004, pp. 993–1000.
- [52] C. Koch and S. Ullman, “Shifts in selective visual attention: towards the underlying neural circuitry,” in *Matters of intelligence*. Springer, 1987, pp. 115–141.
- [53] D. Walther and C. Koch, “Modeling attention to salient proto-objects,” *Neural networks*, vol. 19, no. 9, pp. 1395–1407, 2006.
- [54] R. A. Rensink, “The dynamic representation of scenes,” *Visual cognition*, vol. 7, no. 1-3, pp. 17–42, 2000.
- [55] R. A. Rensink, “Seeing, sensing, and scrutinizing,” *Vision research*, vol. 40, no. 10, pp. 1469–1487, 2000.
- [56] J. Han, K. N. Ngan, M. Li, and H.-J. Zhang, “Unsupervised extraction of visual attention objects in color images,” *IEEE Transactions on Circuits and Systems for Video Technology*, vol. 16, no. 1, pp. 141–145, 2006.
- [57] B. C. Ko and J.-Y. Nam, “Object-of-interest image segmentation based on human attention and semantic region clustering,” *Journal of the Optical Society of America (JOSA A)*, vol. 23, no. 10, pp. 2462–2470, 2006.
- [58] S. Frintrop, M. Klodt, and E. Rome, “A real-time visual attention system using integral images,” in *International conference on computer vision systems*, 2007, pp. 1–10.

- [59] L. Zhang, M. H. Tong, T. K. Marks, H. Shan, and G. W. Cottrell, “Sun: A bayesian framework for saliency using natural statistics,” *Journal of vision*, vol. 8, no. 7, pp. 32–32, 2008.
- [60] V. Mahadevan and N. Vasconcelos, “Background subtraction in highly dynamic scenes,” in *2008 Conference on Computer Vision and Pattern Recognition (CVPR)*. IEEE, 2008, pp. 1–6.
- [61] P. L. Rosin, “A simple method for detecting salient regions,” *Pattern Recognition*, vol. 42, no. 11, pp. 2363–2371, 2009.
- [62] X. Hou and L. Zhang, “Saliency detection: A spectral residual approach,” in *IEEE Conference on Computer Vision and Pattern Recognition (CVPR)*. IEEE, 2007, pp. 1–8.
- [63] J. Harel, C. Koch, and P. Perona, “Graph-based visual saliency,” in *Advances in neural information processing systems*, 2006, pp. 545–552.
- [64] P. Bian and L. Zhang, “Biological plausibility of spectral domain approach for spatiotemporal visual saliency,” in *Advances in Neuro-Information Processing*. Springer, 2008, pp. 251–258.
- [65] A. Torralba, A. Oliva, M. S. Castelhana, and J. M. Henderson, “Contextual guidance of eye movements and attention in real-world scenes: the role of global features in object search.” *Psychological review*, vol. 113, no. 4, p. 766, 2006.

- [66] S. Chopra and K. J. Marfurt, *Seismic attributes for prospect identification and reservoir characterization*. Society of Exploration Geophysicists Tulsa, USA, 2007.
- [67] S. Chopra and K. J. Marfurt, “Seismic attributes a historical perspective,” *Geophysics*, vol. 70, no. 5, pp. 3S0–28S0, 2005.
- [68] R. J. Lisle, “Detection of zones of abnormal strains in structures using gaussian curvature analysis,” *Bulletin of the American Association of Petroleum Geologists (AAPG)*, vol. 78, no. 12, pp. 1811–1819, 1994.
- [69] P. Ruijtenberg and G. Vermeer, “Dip and azimuth displays for 3d seismic interpretation,” *First Break*, vol. 7, no. 3, pp. 86–95, 1989.
- [70] E. Rijks and J. Jauffred, “Attribute extraction: An important application in any detailed 3-d interpretation study,” *The Leading Edge*, vol. 10, no. 9, pp. 11–19, 1991.
- [71] M. T. Taner, F. Koehler, and R. Sheriff, “Complex seismic trace analysis,” *Geophysics*, vol. 44, no. 6, pp. 1041–1063, 1979.
- [72] E. Erdem and A. Erdem, “Visual saliency estimation by nonlinearly integrating features using region covariances,” *Journal of vision*, vol. 13, no. 4, pp. 11–11, 2013.
- [73] “Mathworks kernel description,” <http://mathworks.com/matlabcentral/fileexchange/8214-gray-image-to-color-image-conversion>,.

- [74] R. Rosenholtz, “Search asymmetries? what search asymmetries?” *Perception & Psychophysics*, vol. 63, no. 3, pp. 476–489, 2001.
- [75] R. Rosenholtz, “A simple saliency model predicts a number of motion popout phenomena,” *Vision research*, vol. 39, no. 19, pp. 3157–3163, 1999.
- [76] A. Torralba, “Modeling global scene factors in attention,” *Journal of the Optical Society of America (JOSA A)*, vol. 20, no. 7, pp. 1407–1418, 2003.
- [77] O. Tuzel, F. Porikli, and P. Meer, “Pedestrian detection via classification on riemannian manifolds,” *IEEE Transactions on Pattern Analysis and Machine Intelligence*, vol. 30, no. 10, pp. 1713–1727, 2008.
- [78] P. Viola and M. Jones, “Rapid object detection using a boosted cascade of simple features,” in *IEEE Conference on Computer Vision and Pattern Recognition (CVPR)*, vol. 1. IEEE, 2001, pp. I–511.
- [79] W. Förstner and B. Moonen, “A metric for covariance matrices,” in *Geodesy-The Challenge of the 3rd Millennium*. Springer, 2003, pp. 299–309.
- [80] Z. Wang, T. Hegazy, Z. Long, and G. AlRegib, “Noise-robust detection and tracking of salt domes in postmigrated volumes using texture, tensors, and subspace learning,” *Geophysics*, vol. 80, no. 6, pp. WD101–WD116, 2015.

Vitae

- Name: Abdulmajid Lawal
- Nationality: Nigerian
- Date of Birth: 29/01/1988
- Email: *abdulmajidlawal101@yahoo.com*
- Permenant Address: No 66 Hassan Gwarzo Street, Gandu Albasa Kano,
Nigeria.